14

Contamination in Manufacturing of Carbon Nanostructures

Rolant Eba Medjo

Department of Physics, Faculty of Sciences, University of Douala, Associate Lecturer of Training School of Teacher Technical Secondary School, University of Douala, Cameroon.

Outline:

Introduction

Carbon is not fundamental for only biological being as it might seem. It is also the vanguard of an important number of other smart pure carbon structures constituting its allotropes, among them graphite and diamond. This last three decades, novel forms of carbon were discovered notably fullerenes, carbon nanotubes, carbon nanofibers and graphene. These new forms are called *Carbon Nanostructures* (CNSs). The chemistry of carbon states that neutral carbon atom is tetravalent and has totally six electrons with four of them occupying the outer orbit. Its electronic configuration is $1s^2 2s^2 2p_x^1 2p_y^1 2p_z^0$ and does not explain some bonding of carbon structures. According to Organic Chemistry, one of the two 2s electrons is promoted to $2p_z$ orbital. So the electronic wave functions for the four weakly bound electrons can mix each others thereby changing the occupation of the 2s and 2p orbitals, since the energy difference between the lower *2s* and the upper *2p* levels is low compared to the binding energy in the chemical bonds. This phenomenon consisting in mixing of atomic orbitals is called *Hybridization*. For carbon atoms, three possible hybridizations occur denoted *sp*, sp^2 and sp^3. The sp^n hybridization is essential for determining the dimensionality of carbon-based framework. Carbon is the only element in the periodic classification table that has isomers from 0 dimension (0D) to 3 dimensions (3D). In sp^n hybridization, (n+1) σ bonds per carbon atom are formed; these σ bonds constitute the skeleton for the local structure of *n-dimensional* allotrope. This wonderful property makes carbon atoms very reactive and allows them to form more than 50 % of knowing chemical compounds or molecules. The novel carbons are full of exciting properties, sparkling and fascinating the imagination of the scientific community.

If structural and topological defects of graphene sheets constituting CNSs are neglected, it is observed markedly other non intrinsic features in CNSs XANES (X-ray Absorption Near Edge Structure) spectra. They are the result of *Contamination* which can be considered as an accidental adsorption of atoms, molecules or radical compounds in sidewalls of CNSs, in agreement with SEM (Scanning Electron Microscopy) and TEM (Transmission Electron Microscopy) analysis, where it is not found bundles of CNSs as it may be, according to literature [1-4]. Among the reasons of the presence of non-intrinsic features in XANES spectra in carbon nanostructures spectra is stated also the presence of catalysts TM (Transition Metal) particles as proved by SEM and TEM.

However, many atoms, radicals or molecules are intentionally adsorbed by carbon nanostructures in a procedure called *Functionalization* [5-9], done in order to enhance or match properties of adsorbing compounds and corresponding nanostructures for special uses of obtained nanostructures. Functionalization and Contamination are similar processes in their chemical dimension, but their origins and their goals are completely different. While the first is desired and programmed, the second is spontaneous, accidental and undesired. CNSs can vary in shape, size, surface area, curvature, chirality, number of walls, and impurities (metal, and amorphous carbon…) all these make sorption to CNSs, a complex phenomenon to elucidate. It is critical to understand the interactions between contaminants and CNSs for both processing hazards and nontechnical applications [3, 10]. The Understanding of these interactions is very important and useful for the risk assessment of carbon nanostructures. Adsorption mechanisms will be better understood if the adsorption studies are performed with efficiency [3, 4, 10-14].

The dreams and aspirations of a great part of human being in the Nanotechnology generation of products are efficiency, strong and accuracy. Nanoscience and Nanotechnology have the obligation to

find pathway to process or to manufacture such products. Its basic building blocks are nanostructures in general and carbon nanostructures or novel carbons in particular. As knowledge of manufacturing of these carbon based nanomaterials increases, it is a great need to focus attention in the quality of the nanomaterials obtained in order to enhance the performance of instruments produced.

The aim of this work is to elucidate the presence of undesirable contaminants on carbon nanostructures manufactured in spite of important growth in the domain, their importance (quantity) and effect. In the first section the manufacturing techniques and different parameters are presented. In the second section, are focused the products synthesized and their analysis using Scanning Electron Microscopy (SEM) and Transmission Electron Microscopy (TEM) images. These images allow the prediction of the presence of chemical compounds adsorbed on carbon nanostructures sidewalls. The third section shows the basic of XANES spectroscopy. The fourth section presents the XANES spectra at K-edge of carbon for obtained CNSs and HOPG, used as reference, and shows the importance in term of quantity of the contaminants adsorbed on sample sidewalls. The measurements are carried at grazing and normal incidences. The last section is the discussion on the contamination and its impact on carbon nanostructures properties.

Synthesis Techniques of CNSs Manufacturing

During the last years, there has been a growing interest on carbon-based nanostructures like fullerenes, carbon nanotubes and carbon nanofibers due to their remarkable and tuneable mechanical, electronic and electrochemical properties [15-17]. Many applications and potential applications have been proposed for these carbon nanostructures devices [18-20]. Among the most promising ones, one can mention: semiconductor devices, sensors, energy storage, energy coversion, surface probe for Scanning Probe microscope (SPM) [21-24], high-strength composites (space and aircraft body parts) and primary source of hydrogen storage media for fuel cells, batteries with improved life [12, 17 and 21]. Another application that is intimately connected to carbon thin films is field emission which we consider according to its importance, in more detail below. Today, plastics, composites, electrical, electronics and energy industries are the main consumers of CNSs.

In 1995, four years after their discovery by Sumio Iijima, some groups reported field emission from carbon nanotubes at low turn-on fields and high current densities. It appeared rapidly that every type of carbon nanotubes (arc discharge, laser vaporization, CVD) outclassed the other carbon materials in terms of emission of fields and emission site density [25]. Most of the activity in field emission studies of carbon films is nowadays focused on nanotubes.

Field emission is a quantum mechanical process whereby electrons can tunnel through a potential barrier in the presence of a high electric field. The general expression for the extracted current is the following:

$$I = aV^2 \exp(-b\frac{\phi^{\frac{3}{2}}}{\beta V})$$

where I is the current, V the applied voltage, ϕ work function and β the field enhancement factor [26].

It requires a low way fit electric field. Such applications include electron microscopes [27] and scientific instrumentation, microwave amplifiers, electron beam lithography systems [28 and 29] and x-ray sources, where electrons emitted from carbon nanostructures cathode are accelerated to several keV and bombard a metal target to produce x-rays [30]. The properties of the X-ray source, such as beam size, crucially depend on the electron source. cold electric-field enhanced (EFE) sources with carbon nanostructures cathodes shows improved performance and have led to portable and miniature X-ray sources for industrial, research and medical applications. Carbon nanostructures are available today for industrial applications in bulk quantities. Several CNSs manufactures produce more than 100 tons per year of MWCNTs for example. This spectacular proliferation of CNSs is the result of the appropriate techniques for growing nanostructured materials. Mayor useful synthesized methods are presented in the following lines.

Chemical vapour deposition

The CNSs growth method using a direct current plasma and hot filaments-enhanced catalytic chemical vapour deposition process can produce large quantities of CNSs [24, 31, 32]. CVD of hydrocarbons over metallic catalysts yields the carbon nanotubes and other carbon nanofibers with diameter varying from 2 to 100 nm depending on the synthesis operating parameters as temperature, kind and size of catalyst. A reactant gas containing carbon is inserted into a vacuum chamber at a given temperature between 600 and 1000 K. In the presence of an appropriate catalyst the gas is decomposed and, in the convenient conditions of temperature and pressure, the carbon can feed the growth of CNSs. Nanostructures grown by CVD are usually not straight and contain an important quantities of defects.

There are many variants of CVD. For the samples used in this study, synthesis was done by Hot Filament Plasma Enhanced Catalytical Chemical Vapour Deposition. The different steps of substrate preparation and CNSs growth are presented in Figure 14.1 [33].

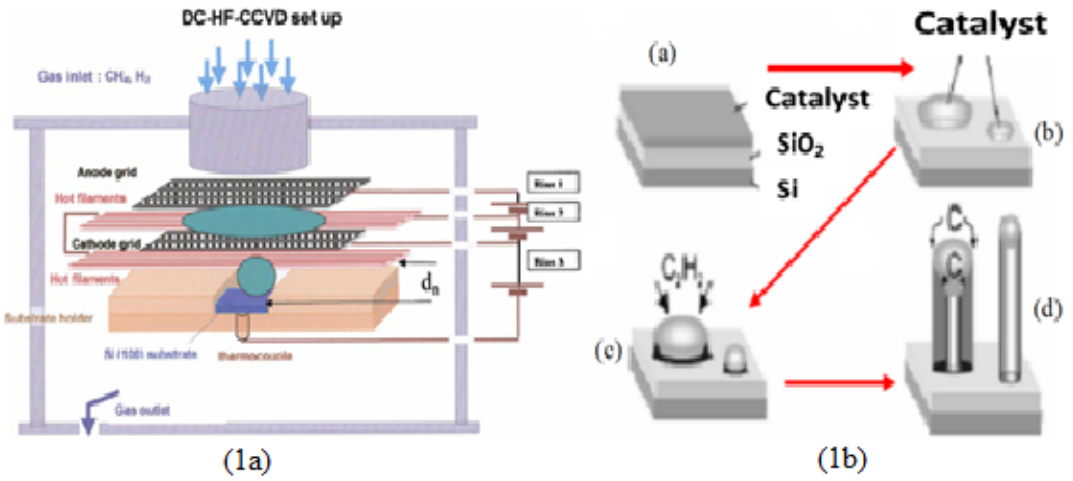

FIGURE 14.1
Representation of the DC HF CCVD system. The distance d_n between the substrate and the bottom of couple filaments is defined. The primary plasma between the cathode and the anode and the extraction plasma above the substrate are displayed in full

Substrate preparation

The substrate is prepared by deposition of a SiO_2 layer (thickness 8 nm) by a Distributed Electron Cyclotron Resonance (DECR) plasma process on a Si(100) sample (Sb n-doped with ρ = 3 mΩ.cm; size 8.5 x 6 x 0.245 mm^3). SiO_2 is evaporated on Si(100) for two main reasons: it is a protective barrier layer that prevents the formation of transition metal silicide through direct interaction with silicon, and SiO_2 is a non-wetting substrate that is convenient for transition metal diffusion and aggregation. However the thickness of the SiO_2 layer must be thin enough to allow electron conduction through tunnelling for field emission measurements. This sample SiO_2/Si(100) was then transferred into a stainless steel Ultra High Vacuum (UHV) preparation chamber (base vacuum 10^{-10} mbar) where transition metal (TM consisting of Co or Fe or a mixture of them) evaporation is performed without air removal. Co (Fe) of 99.995% is evaporated with an OMICRON EFM3 effusive source at a pressure within 7-10x10^{-10} mbar on the sample heated at 925 $\pm$ 20 K during 30 min. The flux rate at 973 K is estimated to 0.025 nm of equivalent layer per minute from an in situ XPS analysis of the Co2p/Si2p signal. Sometimes, the transition metal is deposited by sputtering.

CNSs growth by the DC HF CCVD process

The CNSs growth method using a direct current plasma and hot filaments-enhanced catalytic chemical vapour deposition (DC HF CCVD) process is fully shown in figure 14.1. After the catalyst evaporation, the substrate is further transferred into an UHV CVD chamber for the growth of the carbon nanostructures at base pressure lower than 10^{-9} mbar. The gas mixture (100 sccm (Standard cubic centimetres per minute) C_2H_2:H_2:NH_3) is thermally activated by hot filaments up to a power P_f around 150 W and kinetic energy-activated by polarisation between tantalum grid electrodes with the cathode grid in front of the sample at V_p = -300 $\pm$ 10 V. The discharge is ignited and stabilized by the electron emission of the hot filaments. This ensured a high concentration of ionic species as well as activated radicals in front of the sample. A small additional negative extraction voltage of about V_e = 10 V is applied to the sample, which allowed withdrawing a controlled current of ionic species onto the sample (I_e), with extraction power $P_e = I_e * V_e$. The temperature which value is 973 K is controlled and regulated by an independent infrared heater set on the rear side of the sample. A Pt/PtRh thermocouple is contacted the rear side of the sample during the temperature rise. This thermocouple is switched off when the polarisation is started. The contact is then used to monitor the electric current onto the sample due to the discharge. The sequences of deposition are the following: the sample is first heated under vacuum (10 K/min, 573 K, 10 min). Then the temperature is risen to 973 K (10 K/min; 40 min) in a H_2 atmosphere at 15 mbar. The Acetylene and ammonia were introduced. Subsequently the primary discharge and the extraction discharge onto the sample are adjusted to the desired values. The extraction current I_e is set constant throughout the deposition process. To stop the CNS growth, the acetylene, the polarisation, the filaments and finally the hydrogen feed through are subsequently switched off.

The growth mechanism of CNSs (CNTs, CNFs) occurs cleanly in a process constituting in three steps:

- the adsorption and the decomposition of hydrocarbon species such as CH_4, C_2H_4, C_2H_2 or H_2
- a diffusion of carbon through metallic particles (who settle at the top of the tube in growth) and,

- an extrusion for obtaining the graphitic walls.

According to the nature of hydrocarbon, the mode of deposition of the catalyst as well as the pressure of the gas mixture, the temperature, the hot filaments power and the plasma power, different carbon nanostructures are allowed to grow. The sketch of this process and the draw of the apparatus are given on figure 14.1a.

- The substrate elaboration and growth process are sketched in steps as followed. The growth process starts after the substrate elaboration and proceeds in the vacuum chamber:

- The first step is thermal reduction that occurs at temperature between 30 and 700° C. At this step, the plasma is not yet activated. The formation of transition metal particles begins.

- The second step is the catalyst reduction. It takes place at 700°C under the hot filaments thermal activation. With the activated gas flux of H_2 and NH_3, particles are formed.

- The last step is the growth of the (oriented) CNSs after the addition of the acetylene and ammonia gas always.

From the technologic point of view, CNSs synthesis in general and CNTs in particular aims to optimize field emission and implies the optimization of CNSs films growth in forms of bulk aligned and oriented perpendicularly on a plane substrate. To satisfy these requirements, methods of synthesis by chemical vapour deposition enhanced catalytically by using plasma and hot filaments are considered to be the most versatile [33]. The presence of TM (Fe, Co, Ni) as catalysts spread on the substrate allows controlling local nucleation deeply for oriented CNSs. The choice of transition metals is due to the metal-carbon diagram phase. In the range of temperatures used (700-1200°C), carbon has a finite solubility in these metals, favour the formation of metal-carbon solid solution, segregation and further precipitation. Preparation of metallic particles distribution (size, orientation, density…) is a crucial step of the overview process because the density and the size of TM particles control the size and the distribution of CNSs. To obtain a uniform spatial distribution of TM particles, a proceeding of metal evaporation is done *in situ* under ultra vacuum under lower temperature on SiO_2/Si(100) [33].

Other Synthesis methods

Arc discharge

The arc discharge method, initially used for producing C_{60} fullerenes, is the most common and perhaps easiest way to produce CNSs as it is rather simple. This method is among high temperature processes of carbon nanostructures synthesis. It is probably one of the simplest for synthesizing CNSs on a large scale but it requires purification because products are multimorphological. The most perfect multiwall carbon nanotubes are produced using the arc-discharge evaporation of graphite in an inert atmosphere [31]. However, it is a technique that produces a complex mixture of components, and requires further purification to separate the CNSs from the soot and the residual catalytic metals present in the crude product. This method creates CNSs through arc-vaporization of two carbon rods placed end to end, separated by approximately 1 mm, in an enclosure that is usually filled with inert gas at low pressure. According to recent investigations, it is also possible to create CNSs with the arc method in liquid nitrogen. A direct current of 50 to 100 A, driven by a potential difference of approximately 20 V,

creates a high temperature discharge between the two electrodes. The discharge vaporizes the surface of one of the carbon electrodes, and forms a small rod-shaped deposit on the other electrode.

Laser vaporization

Historically, Laser Ablation or Laser Vaporisation is the pioneering technique used (R. F. Curl, R. E. Smalley and H. W. Kroto). Products quality can be controlled but the method is not suitable for mass production [34]. Laser ablation near the surface of the target creates an almost continuous inflow of hot carbon atoms and ions, into the experimental chamber. The shock wave generated by each pulse rapidly decelerates in the ambient gas atmosphere and further propagation of hot atoms proceeds by diffusion, finally forming a mixture of carbon and filling gas with some average density and temperature. The density and temperature of this mixture change with the distance from the target. The processes of collision, diffusion, and atom-to-atom attachment can be described qualitatively on the basis of a simple kinetic theory [34-39]. Depending on the masses of ablated atoms and the atoms of the filling gas, the processes of energy exchange will occur at different rates. If the masses of colliding atoms are comparable, the carbon can lose a significant part of its energy in a single collision. Hence, efficient energy equilibration occurs after several collisions: the carbon vapour is cooling down and the argon gas is heating up. On the basis of kinetic considerations, the following scenario for carbon nanostructures formation in a carbon-argon mixture created by high repetition rate laser ablation has been suggested.
Initially, the chamber gas is at ambient temperature. The continuous inflow of hot carbon increases the temperature in the mixture. When the carbon vapour temperature and the density reach the level where the probability of carbon-carbon attachment becomes significant, the formation of carbon nanostructures begins. The carbon consumption rate during this formation process significantly exceeds the evaporation rate due to laser ablation. Therefore, the carbon density rapidly decreases to the value where the formation process terminates. Thus, the ablation rate, target parameters, pressure and the ambient gas determine the formation time, and accordingly, the size of the nanostructure. This technique produces CNSs of almost as high quality as arc discharge. The temperatures reached are included in the range of 1200 to 2000 K, which explains the residual difference in graphitization. The schematic diagram of laser ablation apparatus is shown on the figure 14.2 following.

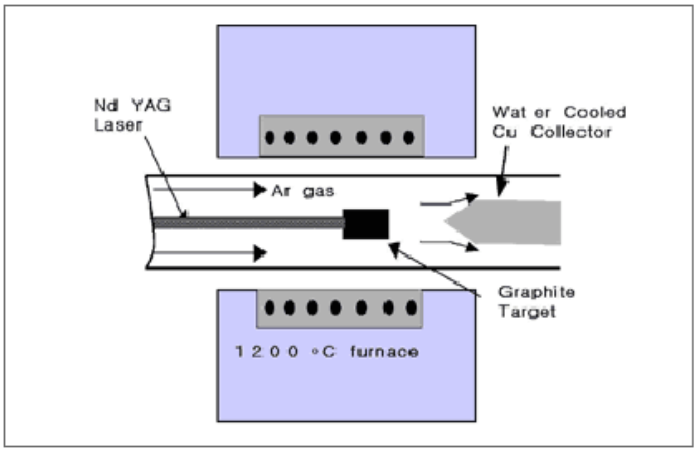

FIGURE 14.2
Schematics of laser vaporization of CNSs synthesis setup

Plasma arcing

This method was the first for producing CNSs in reasonable quantities. It consists on applying an electric current across two carbonaceous electrodes in an inert gas atmosphere. It involves the evaporation of one electrode as cations followed by deposition at the other electrode. This plasma-based process is analogous to the more familiar electroplating process in a liquid medium. CNSs are formed by plasma arcing of carbonaceous materials, particularly graphite. The fullerenes appear in the soot that is formed, while the CNTs are deposited on the arcing in the presence of cobalt with a 3% or greater concentration. However, when cobalt is added as a catalyst, the nature of the product changes. The mechanism by which cobalt changes this process is still unclear.

Ball miling

Essentially, this method consists of placing graphite powder into a stainless steel container along with four hardened steel balls. The container is purged, and argon is introduced. The milling is carried out at room temperature for up to 150 hours. Following milling, the powder is annealed under an inert gas flow at temperatures of 1400 °C for six hours. The mechanism of this process is not well known, but it is thought that the ball milling process forms nanostructures nuclei, and the annealing process activates nanostructures growth

Flame Synthesis

A fuel-rich flame is a high-temperature carbon-rich environment that can be suitable for nanostructures formation if transition metals like Fe, Co or Ni are introduced into the system. As such, flame synthesis is a continuous-flow, scalable method with potential for considerably lower cost nanostructures production than is available from other methods.
Flame synthesis is recognized as a much cheaper and higher throughput process for carbon nanotube/nanofiber production [40-43] compared to conventional catalytic processes like chemical vapour deposition. The control of the morphology and the structure at the nanometer scale of those carbon nanomaterials is still an ongoing challenge. A better understanding of the deposition processes and nanostructures relationship requires advanced characterization techniques. Contributions dealing with characterization techniques of bulk and surface are solicited to address these critical materials issues.

Carbon Nanostructures obtained by the HF PE CCVD process

It is well known that synthesis parameters like temperature, kind and size of catalyst and synthesis technique are of great importance in manufacturing carbon nanostructures in general [32]. Different carbon nanostructures are allowed to growth according to the nature, the mode of deposition of the catalyst as well as the pressure of the gas mixture, the temperature, the hot filaments power and the plasma power in DC HF CCVD for example. Figure 14.3 and figure 14.4 present scanning electron microscopy (SEM) and transmission electron microscopy (TEM) respectively, for carbon nanostructures synthesized. Tables 14.1 and 14.2 give experimental parameters and variable CNSs obtained.

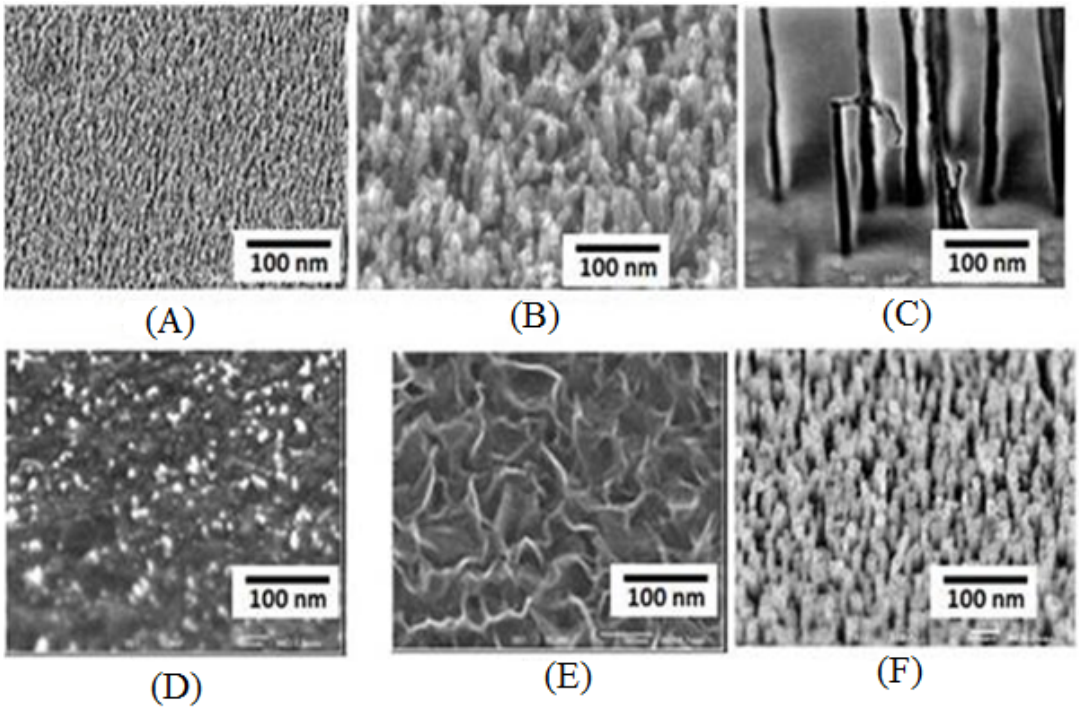

FIGURE 14.3
SEM images of CNSs obtained on XL30S-FEG PHILIPS working at 3 kV: (A) Forest of CNTs poorly oriented in low magnitude; (B) CNFs poorly oriented; (C) CNFs medium range orientation; (D) CNPs; (E) CNWs; (F) CNTs highly oriented

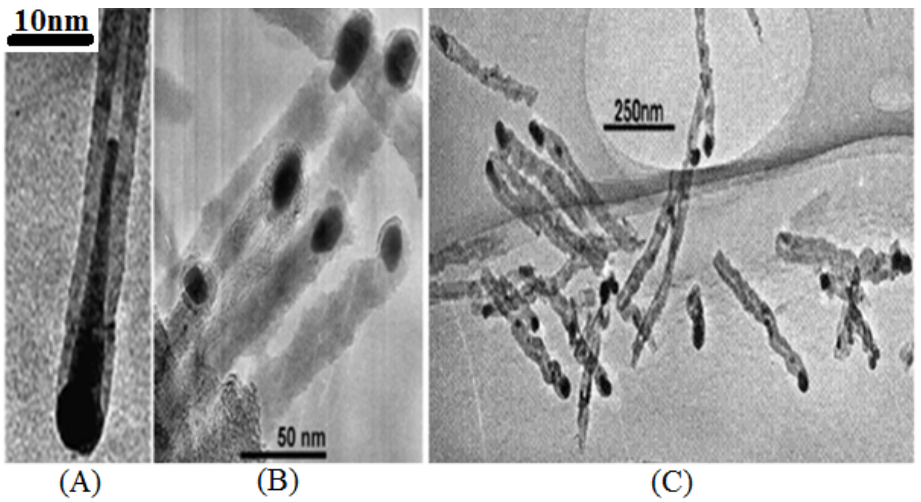

Figure 14.4
Overview of CNTs TEM images of samples synthesized with 1% of NH_3, with TM particles inserted at one end: (A) CNT highly oriented; (B) CNTs medium oriented and (C) CNTs with the two ends detached from the substrate. One end has graphitic structure (half-fullerene) and the other has a TM particle inserted in the tube

The catalyst preparation and concentration

Often the catalyst consists of transition metals: Fe, Co, Ni or a mixture of them. Two methods of catalyst deposition are used, the evaporation or the sputtering as shown in Table 14.2. The measurement of the quantity of catalyst deposited is given by the surface ratio, catalyst/Si, Co/Si for example. In this synthesis, the transition metal used is Co or the mixture of Co-Fe.

Growth conditions

There is an important number of parameters which define the growth conditions. The four determinative are: the temperature, the plasma power P_e, the filaments power P_f and the pressure. Table 14.1 reports the main conditions and catalyst preparation mode. According to this table, the carbon nanofibers are synthesized under different conditions. When the plasma power is high and the catalyst surface concentration low, the graphene sheets grow in a direction normal to the surface, forming conical carbon nanostructures with the catalyst metal particle on top of each carbon nanofiber on top growth mode. When the catalyst is prepared by sputtering and the plasma power rather low, the CNFs can grow with graphene sheets axis parallel to the surface. Strong adhesion of the catalyst to the substrate and low energy ions can explain this mode of growth. Carbon nanoparticules (CNPs) are prepared when the power of the hot filaments is low. The growth of graphene layer seems impossible. The incorporation of nanoscale carbon materials into electrodes serves to increase electrode performance for specific applications. Modification of carbon paste electrodes with CNSs is frequently employed and serves as a material of choice for a variety of microelectrophysiological measurements and electroanalytical detection techniques and applications, including electrochemical detection of microfluidic separations [44], scanning electrochemical microscopy [45].

TABLE 14.1
Main experimental growth parameter of Carbon nanostructures samples (* Plasma parameters free to vary, ** Plasma parameters allowed to vary), sccm (standard cubic centimetre per minute)

Parameters			
	0% NH3	**1% NH_3**	**3% NH_3**
Temperature of substances (K)	973	973	973
$C_2H_2 + NH_3 + H_2$ (sccm)	100	100	100
C_2H_2 (%)	20	20	20
P (mbar)	15	15	15
NH_3 (%)	0	1	3
t (minutes)	15	15	15
Activation power of the filaments (W)	150	150	150
[Temperature of the filament (K)]	[2100]	[2100]	[2100]
d_n (mm) Substrate-Filaments distance	5	5	5
V^*_P (V) DC Activation	310	300	295
I_P* (mA) DC Activation	3.75	11	16
V_e** (V) extraction (V)	10	10	10
I_e** (mA) extraction	2	2	2

Table 14.1 shows the three ammonia concentrations introduced in gas mixture during the synthesis. These concentrations are 0, 1 and 3% respectively. The acetylene concentration remained at 20%. Hydrogen is the third and last gas in the mixture. The pressure inside the chamber is 15 mbar during the 15 minutes which are the duration of synthesis. The activation power of the filaments is 150 W and yields the filaments temperature of 2100 K. The distance d_n between the substrate and the bottom couple of filaments is 5 mm.

Carbon obtained

Different carbon nanomaterials synthesized are resumed in table 14.2 with their mayor parameters. This table reveals that CNTs is the most probably synthesized product because it is obtained with many parameters combinations. "Single walled carbon nanotubes come often as tightly bundles of single walled nanotubes entangled as curly locks" is often seen in literature. The packing of nanotubes inside a bundle is not observed in specific case, helping to differentiate SWCNTs from MWCNTs. CNTs are simply observed in SEM images as tubes forest with poorly, medium or high orientation depending on synthesis conditions, in particular the concentration of ammonia. It is possible that CNTs grown by HF PE CCVD be only MWCNTs. The second hypothesis is that defects, TM particles or contaminants in nanostructures sidewalls, preclude SWCNTs present to gather in bundles. The third assumption can be that SWCNTs are present in samples, but these CNTs cannot form bundle because of orientation problems. TEM observations present CNSs with no clean surface. Carefully observation of CNSs surface allows the presence of absorbate compounds.
The disorder that affects the immediate appearance of CNSs TEM in high resolution imaging is mainly due to materials adsorbed on their outside walls or incorporated into the cylindrical hollows. Beyond mere appearances, these contaminants substantially change the chemical and physical properties of bulk material.

TABLE 14.2
Carbon nanostructures grown on SiO_2(5nm)/Si(100) substrate and main preparation characteristics. Other conditions are: 100 sccm C_2H_2:H_2:NH_3 with relative content 20:79:1, filaments- substrate distance is 5mm; gas flow: 100 sccm, P_f (filament power) and P_e (extraction power).

Sample	Catalyst	TM deposition Process	**Carbon Nanostructure**	TM/Si	P_f (W)	P_e (mW)	Pressure (mbars)	T (K)
I	Co	Sputtering	**CNFs (graphene // substrate)**	/	150	10	15	973
II	Co	Sputtering	**CNTs (poorly oriented)**	/	150	30	15	973
III	Co	Evaporation	**CNFs (graphene $\perp$ substrate)**	0.33	150	30	15	973
IV	Co	Evaporation	**CNTs**	0.87	150	30	15	973
V	Co	Evaporation	**CNPs**	/	100	20	15	973
VI	Co	Evaporation	**CNTs (highly oriented)**	/	145	20	15	1083
VII	Co	Evaporation	**CNTs (medium oriented)**	/	140	20	15	973
VIII	Co-Fe	Evaporation	**CNTs (highly oriented)**	/	140	20	15	973
IX	Co	Evaporation	**CNWs**	/	140	20	5	973

X-ray absorption near edge structure spectroscopy

Base

X-ray absorption near-edge structure also called NEXAFS for Near-Edge X-ray Absorption Fine Structure exists in the energy level of 50 eV around the absorption edge. It includes the unoccupied part of band structure just above the Fermi level. Thus, certain aspects of electronic structure of detected element can be revealed. XANES spectroscopy at edges gives information about the unoccupied states. Carbon atoms for example, are distributed in a perfect hexagonal network in carbon nanostructures with sp^2 hybridization, and those constituting defects should be different in their electronic states and an increasing of the defects portion in any material will have stronger effect on their electronic structure. The measured energy and density of electronic states can be directly related to the results of quantum-chemical calculations. In XANES region, photoelectrons populate unoccupied states above the Fermi level, the densities of the final states change because of the scattered waves and the shapes of the absorption edges of the same element in different chemical environments are quite different. Figure 14.5 shows strong dependence of the shapes of the spectra on the atoms among which Zn resides. As an example, the K-edges XAS spectra of zinc in zinc oxide, zinc metal, diethyl of zinc and monatomic vapour zinc are quite different as illustrated in Figure 14.5. The shape of Zn vapour cannot be explained using the MS theory, but it can be decomposed unto separate contributions of well known shapes [46, 47]. An electron with low kinetic energy is scattered strongly and many times by neighbouring atoms, in contrast with single scattering which prevails in the high energy region. Multiple scattering depends strongly on angles between scatterers and is thus very sensitive to local environment of the absorbing atom [48, 49]. The *muffin-tin approximation* leads to calculated spectra of XANES in general agreement with improvement. The shape of the XANES spectra depends mainly on the structure of the matter and less on detailed properties of potentials used in *muffin-tin approximation*. Furthermore, specific calculations require substantial computing power.

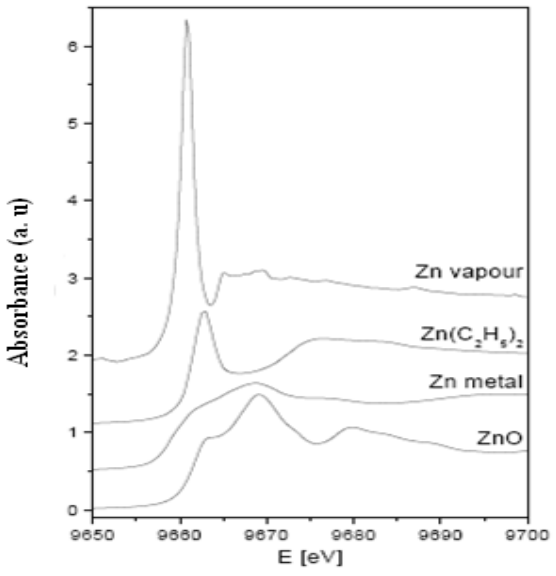

FIGURE 14.5
XANES spectra of K-edge of Zn oxide, Zn metal, Zn-diethyl and Zn vapour

XANES spectra

Background

To ascertain the reliability of the quantitative CNSs XANES spectra analysis performed, the starting point is the drafting of XANES spectra of the HOPG serving as a model reference. Graphite with its layered structure and large interlayer separation is often modelled as a two-dimensional solid [50]. As a consequence, it has been the subject of a great deal of experimental and theoretical work. In addition, knowledge of the properties of graphite is a starting point for harnessing and understanding of carbon nanostructures, and deposit properties. The two-dimensional nature of graphite results in a strong directionality of the orbitals: σ orbitals lie within the basal plane, while π orbitals are directed perpendicular to the basal plane. By using tuneable, polarized synchrotron radiation, it is possible to excite final states of specific symmetry from K-shell initial states.

When the **E** vector lies within the basal plane, σ final states are selected, while when the **E** vector is perpendicular to the basal plane, states of π symmetry are excited. The use of the polarisation-dependent carbon K near-edge x-ray absorption fine structure and the density of states calculations has made it possible to assign these features to particular Brillouin-zone regions in the theoretical band structure of graphite [51, 52]. Thus, by monitoring the angular variations of the spectral features of the carbon K NEXAFS spectrum, the symmetry of the final states of HOPG (High Oriented Pirolytic Graphite) were determined. The spectral features arise from transitions of a carbon 1s electron to states of σ– or π- symmetry and dipole selection rules may be used to understand the angular dispersion of the peak intensities. It is shown that, the transitions are $1s \rightarrow \sigma$ for **E** $\perp$ **c** and $1s \rightarrow \pi$ for $//$ **c** where **c** is the vector normal to the surface. For electric dipole transitions excited by polarized radiations, the intensity varies as $\sin^2\sigma$, where α is the angle between the Poynting vector and the surface normal. Therefore, in the single–crystal graphite, the intensity of a pure $1s \rightarrow \pi$ transition is shown to be proportional to $\sin^2\sigma$, with its maximum at grazing incidence, while the intensity of a pure $1s \rightarrow \sigma$ transition is shown to be proportional to $\cos^2\sigma$ with its maximum at normal incidence.

Assignments of peaks of Graphite (HOPG)

Figure 14.6 shows experimental and calculated superimposed XANES spectra at grazing and normal incidences. As a result of these treatments, the energies and assignments of the main peaks in the carbon K-edge excitation spectrum of single-crystal graphite as well as their final-state bands and Brillouin-zone regions are summarized elsewhere [51]. The two prominent peaks A and B at 285.5 eV and 292.5 eV are known to be associated with unoccupied π* band called *white band* and σ* band, respectively [53]. Their final-states band and Brillouin-zone region are π_0 near Q and σ_1, σ_2 at $\Gamma \rightarrow$ Q, respectively. Between the π* and σ* peaks, two weak peaks near 287.5 and 285.5 eV, are currently observed in the XANES spectra of graphite. These features were attributed to the free-electron-like interlayer (FELI) states in the graphite and they are of σ-symmetry [54]. Also not mentioned this reference, some HOPG XANES spectra exhibit aσ* exciton at 291.63 eV corresponding to a C-H* bond resonance.

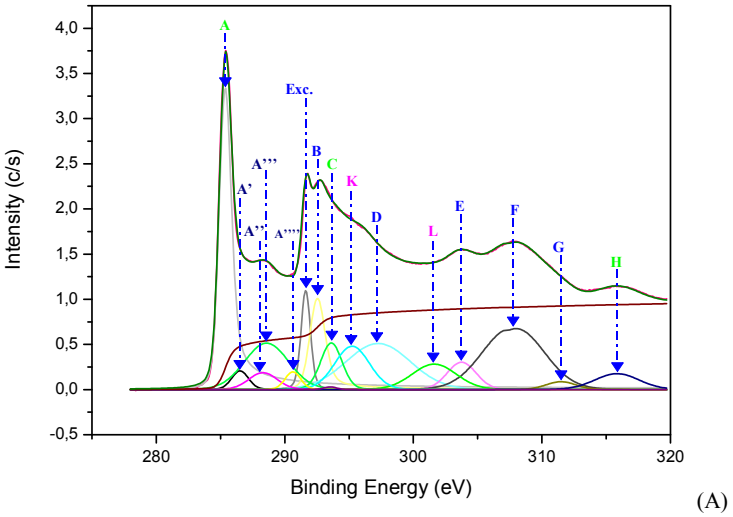

(A)

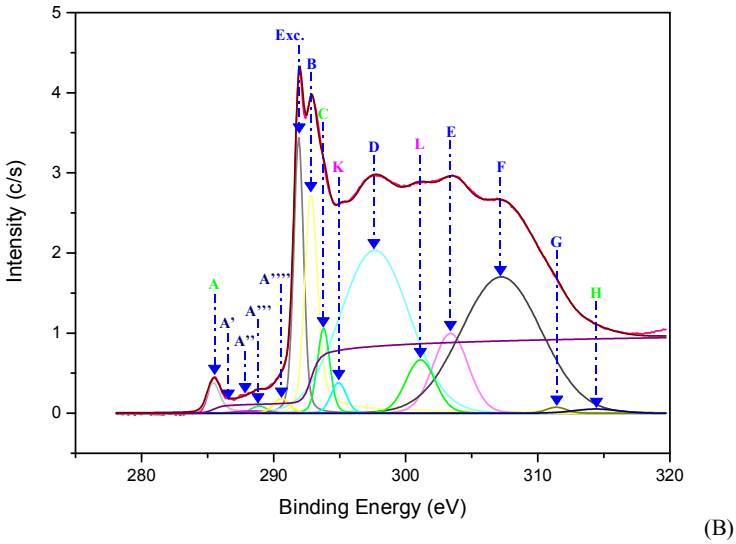

(B)

FIGURE 14.6
HOPG experimental and calculated superimposed XANES spectra: (A) grazing incidence (B) normal incidence

The carbon spectral feature at 295.5 corresponds to a π_0 or π_1 final state near Γ with a π-symmetry. The D band around 297.8 eV is correlated to the σ_3-σ_6: $Q \rightarrow P$ band with σ symmetry. The E feature at 303.5 eV is related to the σ_7 final state near Q Brillouin-zone and is of σ-symmetry. The F structure at 307.5 eV is of σ-symmetry corresponding to a σ_9 final state near Q [55, 56]. The H peak at 316.5 eV corresponds to π_4 final state near the Q Brillouin zone with a π-symmetry. For the peaks G(308.5 eV), I(329 eV) and J(333 eV), an unambiguous determination of the symmetry was not possible from the XANES spectra. Inadequate energy resolution and uncertain normalization result in uncertainties in the peak intensities.

In Figure 14.6 are sketched HOPG XANES spectra collected at grazing incidence and normal incidence respectively. Table 14.3 presents the corresponding energies and assignments as well as the corresponding final-state bands and Brillouin-zone regions.

Consistently, in fair agreement with the literature, the spectrum is dominated by the π^* band and the π-symmetry final-state structures C and H are well resolved, the H one presenting its maximum intensity at 316.5 eV. In addition, the σ-C-H* exciton at 292 eV and the free-electron-like interlayer states at 286.5 and 288.5 eV not observed and nor mentioned by Rosenberg *et al*., but observed in reference [54] are well resolved in the present spectra.

TABLE 14.3
Main features' parameters for HOPG XAS spectrum at grazing incidence and derived from figure 14.6

HOPG at Grazing					
Peaks' Names	Peaks	Binding energy (eV)	Kinetic energy (eV)	Intensity (c/s)	Final-state band and Brillouin-zone
A	285.50	285.38	1199.02	7.40	π_0 near Q
A'	286.53	286.60	1197.80	0.36	free-electron-like interlayer states + adsorption
A''	288.40	288.40	1196.00	0.54	free-electron-like interlayer states + adsorption
A'''	288.70	288.68	1195.72	2.28	free-electron-like interlayer states + adsorption
A''''	290.70	290.75	1193.65	0.32	free-electron-like interlayer states + adsorption
C-H Exc.	291.76	291.76	1192.64	1.12	Exciton
B	292.65	292.63	1191.77	2.30	σ_1, σ_2: $\Gamma \rightarrow$Q
C	295.50	293.77	1190.63	1.13	π_0 or π_1 near Γ
D	297.80	297.45	1186.95	3.28	σ_3–σ_6: Q$\rightarrow$P
E	303.50	304.00	1180.40	0.89	σ_7 near Q
F	307.50	307.86	1176.54	3.88	σ_9 near Q
G	308.50	311.40	1173.00	0.26	/
H	316.50	315.80	1168.60	0.78	π_4 near Q
I	329.00	329.00	/	/	/
J	333.00	333.00	/	/	/
K	295.40	295.40	1189.00	1.68	π_0 or π_1 near Γ
L	301.85	301.85	1182.55	1.25	σ_6–σ_7: near Q

Furthermore, the FELLI states band may be somewhat intense. This contribution to the intensity steams from adsorption state related to no previous annealing of the sample before recording the XANES spectra. Tables 14.3 and 14.4 show the main features of XANES spectra of HOPG in grazing and normal incidences. Dramatic changes occur with incidence of the polarisation radiation onto the substrate, as displayed in figure 14.6. At normal incidence, the carbon 1s $\rightarrow \pi^*$ transition A almost disappears, consistent with the orthogonality of the electric field vector with the orientation of the π^* orbitals. The

small intensity of peak A observed may be explained by incomplete polarisation or by a small sample misalignment.

Assignments of peaks of CNSs

The intensive investigation of the formation of CNSs found that it depends deeply on initial chemical states of carbon atoms and the specific type of TM. The use of metallic catalysts gave an improved nanomaterials yield [32]. TM catalysts were reported to come into close contact with the tube walls and significantly influence the transport properties of nanostructures [57]. Theoretical investigations revealed that carbon atoms in the graphite sheet interact strongly with the TM particles and there is a strong hybridization between C2p and TM d orbitals. The charge transfer, from carbon to TM effect and the magnetic momentum of the TM atoms were found to depend strongly on the metal-graphite interlayer distance and adsorption site [58].

The curvature of the graphite sheet is also among those factors that were considered to explain the change of the electronic states in CNSs [59]. The carbon K-edge absorption [51, 54] and TEM [60] revealed that the features of electronic states of the carbon atoms in the carbon nanostructures are very similar to those of graphite. Thus, the CNSs XANES spectra are very similar to those of graphite and almost identical with that of HOPG measured at a certain incidence angle. However, taking into consideration a random orientation of the CNSs, the spectrum should be compared with that of HOPG measured with incident angle of 55° near the magic angle where there is no polarization dependence of π-type states on the x-ray beam. The comparatively low intensity of the $1s \rightarrow \pi^*$ transition in the XANES spectrum of nanostructures may be attributed to the curvature of the sheets which reduces the interaction among π orbitals in the nanostructures. In the fitting procedure, the energy is quoted to 0.21 eV. It is clear that the occurrence of the transitions is related to the unoccupied density of states (UDOS) and to final state effects. The full carbon K-edge absorption spectra of CNSs as observed in Figure 14.7 to Figure 14.8 can be divided into three regions.

The first region is located at 285.5 eV with the peak named A. This peak corresponds to the transition towards unoccupied π_0 states near Q in the Brillouin zone at 2 eV above the Fermi level [51, 52 and 61].

The second region within 286.5-290.5 eV corresponds to the free electron like interlayer states [52, 61] and adsorbed or chemisorbed molecular states [61]. They are strongly dependent on the chemical treatment of the sample before and after an in situ thermal treatment at 500°C. In this energy range, the contributions of $1s \rightarrow \pi^*$ and $1s \rightarrow \sigma^*$ transitions are due to adsorbed functionalized states such as C-O-, C-H, C=O, C-OH… They are due to the adsorption of various molecules like H_2O, CO, CO_2 or hydrocarbons. For example, HOPG XANES spectra exhibit a σ* exciton at 291.6 eV corresponding to a C-H* bond resonance [54, 56 and 61]. The presence of σ* exciton at 291.6 eV points to a material with well-formed local bonding configuration or good short-range order. Figures 14.7 and 14.10 show XANES experimental and calculated superimposed spectra at normal and grazing incidences from annealed samples of CNSs respectively. The small shoulder at 286-287 eV may also be attributed to a singularity in the density of states (DOS) of graphite [51]. The third region above 291.8 eV corresponds to transitions towards empty states of σ* and π^* symmetry states. Moreover, the angular dependence allows to distinguish between σ* symmetry from π^* symmetry states. Thus at a grazing incidence ($\pi/2-\alpha = 15°$), in addition to the peak A, other transitions with a π-symmetry are involved in transitions named C and H at 295.5 eV and at 316.5 eV which might correspond to π_0 or π_1 final states near Γ and to π_4 final state near Q in the Brillouin zone, respectively. In agreement with these assignations these

contributions are maxima at this incidence angle. Reversely from the normalized carbon K-edge spectrum of HOPG at normal incidence (Figure 14.6B), the B, D, E, F and G spectral features at 292.5 eV, 297.8 eV, 303.5 eV, 307,5 eV and 311.4 eV, respectively, are mainly transitions to the σ^* unoccupied final states. They are σ_1, σ_2; σ_3-σ_6; σ_7; σ_9 and σ_{10} states in the Brillouin zone $\Gamma \rightarrow Q$, $Q \rightarrow P$, and near Q, respectively. Other small contributions due to the resonance of σ^* transitions of adsorbed molecules can be present around 300 eV and around 296.5 eV, but they are believed to be negligible after heat treatment. These main features are summarized in Table 14.11 and Table 14.12. There are some non-intrinsic features in XANES spectra, some disappeared or became weak after thermal annealing, among them are P, P' and P" resulting on potassium contamination.

In the high energy range, contributions to multiple and single scattering interfere with the transitions. The analysis becomes critical and has not been continued above 320 eV.

Contamination of CNSs detection using XANES spectra

Sorption Properties of CNSs

Although graphene layer is relatively inert and clean, it would be incorrect to conclude that CNSs are clean or adsorbate-free. Even hydrophobic sheets can have adsorbed atoms, molecules and compounds such as H_2O H or O. Soluble gases and contaminants, including alkali salts and hydrocarbons, will also adsorb onto these walls. The comparison of graphite and CNSs shows three main differences suggesting that CNSs are even more sensitive to adsorbates than graphite surface.

First of all, the presence of curvature in graphene sheets of any carbon nanostructure gives born to partial sp^3 hybridization of carbon atoms, accentuated in SWNTs because of its great curvature, enhances the π electron density on the sidewall.

Secondly, curvature also frustrates dense packing of CNSs. Whether bundled together, settled onto a wall, or packed into a pellet, these carbon-based novel materials have enhanced specific surface areas comprised of physically interconnected, interstitial voids. Adsorbate compounds in these voids can be better coordinated than on flat graphene surfaces, and the voids readily accommodate a wider range of molecular shapes and sizes than do interlayer graphite interstices [62-64].

And finally, every atom in a hollow CNSs is a surface atom, and the addition of adsorbates is a proportionally larger perturbation in CNSs than in solid materials. Carbon nanostructure should not be considered as simple carbon lattice. In fact, carbon lattice interacts easily by chemisorption with O_2^- or physisorption with hydrocarbons. In low-scale context, the effects of these adsorb compounds can be very important because of the *breaking the symmetry* of the structure and physically extend the system away from an idealized one dimension line.

Manufacturing processes

Manufacturing into vacuum combined with annealing processes are insufficient precautions to remove or to solve the problem of sidewall adsorbates in CNSs. Once synthesized, the subsequence manipulations of CNSs into a useful state always involve extensive chemical and mechanical processing leading to changes on CNSs surface and often creates new defection sites. Any meaningful evaluation

of these induce problems and their consequences must be in the context of processing priorities and, consequently among prior targeted views of applications.
The first type of processing that tends to improve CNSs crystallinity matches the vacuum operating and thermal annealing effectively at 1200–1500 °C.
The second type investigates the interaction between acids and graphitic materials. Strong acids such as HNO_3 and H_2SO_4 do not continuously etch graphene's surface and instead covalently add to its edges and basal planes. On CNSs sidewall, covalent adducts constitute a new type of defects. The adduct defect occurs when a single carbon atom rehybridizes to a sp^3 conjugation, forming a new bond perpendicular to the sp^2 basal plane. All chemical processing can be divided into two categories: attempts to purify the CNSs and attempts to modify their surfaces. In the latter, the processing is designed to chemically attack the CNSs sidewall. Acid treatments are usually combined with additional oxidants, heating, and ultrasound treatments to produce different stable and permanent functional compounds. But, the resulting materials are highly defective once cleaned in this manner. For example, CNSs are routinely imaged by SEM and exposed to high electron doses in the electron beam lithography process. A long standing problem in CNSs synthesis continues to be the quantitative evaluation of purity, either before or after additional purification or processing. Transition metals help catalyze CNSs growth and are required in all methods of growth. Post synthesis, the metals are difficult to remove: they are often encapsulated by many spherical layers of graphitic carbon, and they can be in the form of pure metals, carbides, or oxides. Some metal sites at the tips of CNSs, or inside the endcaps of MWNTs, where complete removal requires extensive etching of the caps and concurrent sidewall damage. When present, these residual metals modify most observable bulk properties – electrochemical activity, thermal stability, surface area and density, magnetic susceptibility. Mesoscopic graphitic carbons are a second primary contaminant in CNTs. Without purification, the residual catalyst metals remained in bulk of nanomaterial and reduce its oxidation threshold. Of course their presence reduces and broadens substantially the temperature range over which bulk material burns. While the introduction of defects and contaminants is plastic and generally nonreversible, their mechanical consequences are not as substantial as their electronic effects. The variety of allowed morphological deformations reduces the likelihood of brittle fracture in CNTs, and results in a physical behaviour remarkably similar to macroscopic polymers.

XANES Spectra of CNSs at normal incidence

XANES is among the most powerful technique in resolving and detecting the bonding environment of atoms in molecules and clusters, because of its high sensitivity to the geometrical environment around the absorbing atom and its medium range vicinity. Many other spectroscopies are central to the characterization of carbon-based materials. Using the fingerprint spectra, CNSs are identified (diameter, chirality, and electronic structure…), spectral features also help to qualitatively evaluate purities. For example, in the case of FTIR, many chemical compounds are identified by unique peaks. Single C-O bonds due to hydroxyl terminations occur at 1190 cm^{-1}. The double C=O bonds of carboxylic groups are found at 1720 cm^{-1}.

Pristine CNSs

The energies and assignments of the main peaks in the Carbon K-edge spectra of pristine CNSs at normal incidence are summarized in table 14.4. The two prominent peaks near 285.5 eV (A) and 292.5 eV (B) are known to be associated with an unoccupied π^* band or 'white band' and σ^* band, respectively.

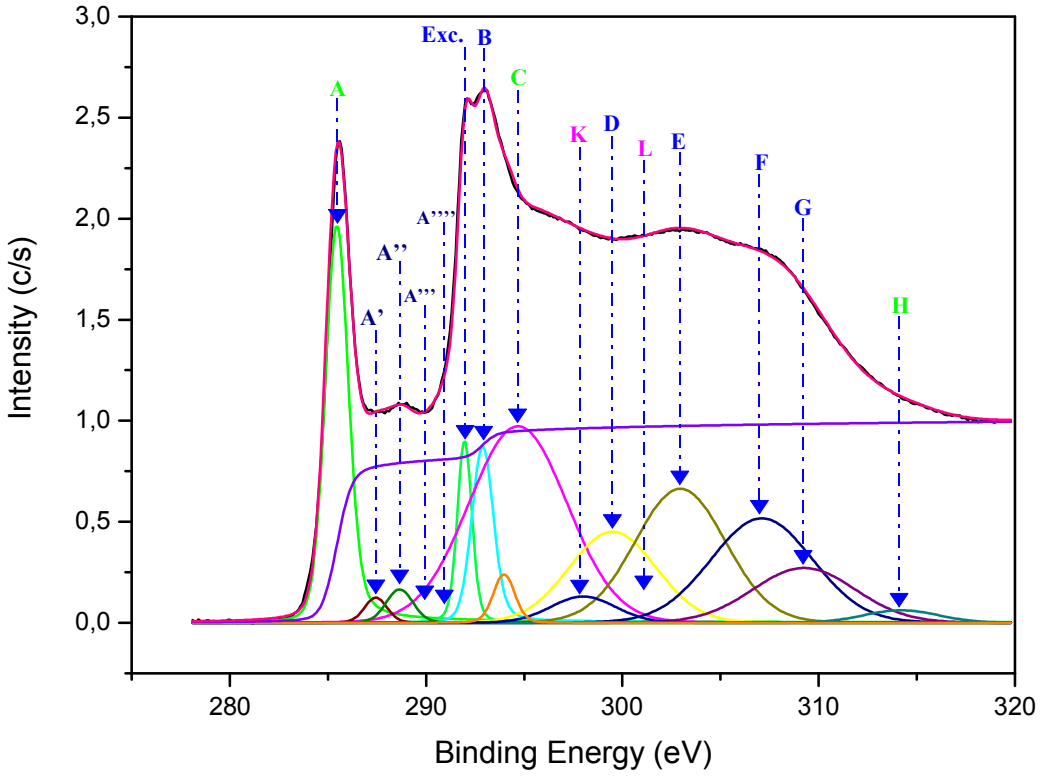

FIGURE 14.7
CNSs experimental and calculated superimposed XANES spectra at normal incidence from the CNTs Annealed sample

The C spectral feature at 293.77 eV corresponds to a π -symmetry. The D, E and F peaks around 297.8, 305.5 and 307.5 eV, respectively, are correlated to σ -symmetry. The H peak at 316.5 eV corresponds to π -symmetry. For peaks G, I and J, respectively, at 308.5, 329 and 333 eV in [51], an unambiguous determination of the symmetry was not possible from the XANES spectra. Inadequate energy resolution and uncertain normalization result in uncertainties in the peak intensities. Consistently, in good agreement with the literature studies, the spectra are dominated by the σ∗- and σ -C H∗- bands, and the σ -symmetry final-state structures B, D, E and F are well resolved. The H π -symmetry final state observed at grazing incidence and located at 316.5 eV has completely disappeared at normal incidence. The σ -C H∗ exciton at 292 eV and the free-electron-like interlayer states at 286.5 and 288.5 eV are well resolved in figure 7.

TABLE 14.4
Main features' parameters for annealed CNTs XAS spectrum at normarl incidence

CNTs at normal incidence for annealed					
Peaks' Names	Peaks	Binding energy (eV)	Kinetic energy (eV)	Intensity (c/s)	Final-state band and Brillouin-zone
A	285.50	285.43	1198.97	3.44	π_0 near Q
A'	286.53	287.54	1196.96	0.19	free-electron-like interlayer states + adsorption
A''	288.40	288.65	1195.75	0.30	free-electron-like interlayer states + adsorption
A'''	288.70	/	/	/	free-electron-like interlayer states + adsorption
A''''	290.70	/	/	/	free-electron-like interlayer states + adsorption
C-H Exc.	291.76	291.96	1192.44	0.92	Exciton
B	292.65	292.86	1191.54	1.40	σ_1, σ_2: $\Gamma \rightarrow$Q
C	295.50	294.68	1189.72	6.20	π_0 or π_1 near Γ
D	297.80	299.10	1186.40	0.55	σ_3–σ_6: Q$\rightarrow$P
E	303.50	302.95	1181.45	3.88	σ_7 near Q
F	307.50	307.10	1177.30	3.40	σ_9 near Q
G	308.50	309.25	1175.15	1.80	/
H	316.50	314.20	1170.20	0.30	π_4 near Q
I	329.00	329.00	/	/	/
J	333.00	333.00	/	/	/
K	295.40	297.05	1187.35	0.00	π_0 or π_1 near Γ
L	301.85	299.50	1184.90	2.54	σ_6–σ_7: near Q

Annealed contaminated CNSs

Prior annealing of some samples has prevented the increase of intensity in the free-electron-like interlayer states band region of the spectra, suggesting that these peaks are not intrinsic to the CNT spectra, but the result of a surface contamination. Figure 14.8 shows the main features of XANES annealed spectra of potassium CNTs contaminated.

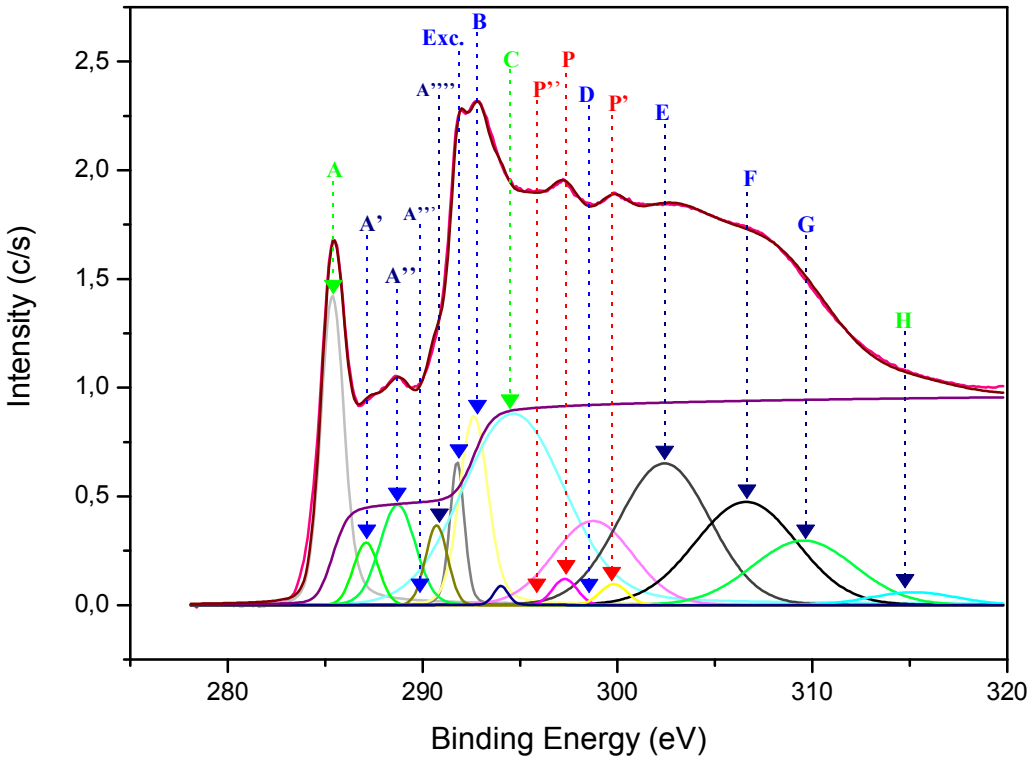

FIGURE 14.8
Potassium contaminated CNTs experimental and calculated superimposed XAS spectra at normal incidence from the annealed sample of CNTs

The $\pi*$ antibonding state corresponds physically to the out-of-plane bonds in the sp^2 bonding configuration (indicating the presence of unsaturated carbon–carbon interactions) and exhibits strong polarization dependence. The presence of a $\sigma*$ exciton at 292 eV points to a material with well-formed local bonding configuration or good short-range order and exhibits long-range disorder. The planar graphite sheets in the nanotubes are bent into a cylinder. While varying the diameter of the CNTs, the intensities of the $\pi*$ -band and interlayer-states features are enhanced relative to those of HOPG with a decrease of the CNT diameter. The increase of the near-edge feature intensities with the decrease of the CNT diameter suggests that both the C2p orbitals lose more charge to the 3d orbitals of the catalyst transition metal (TM) atoms: nickel, cobalt and iron, for smaller-diameter CNTs and the presence of surface contaminants.

TABLE 14.5
Main features' parameters for annealed and potassium-contaminated CNTs XAS spectra at normal incidence

Annealed and potassium-contaminated CNSs at normal incidence					
Peaks' Names	Peaks	Binding energy (eV)	Kinetic energy (eV)	Intensity (c/s)	Final-state band and Brillouin-zone
A	285.50	285.35	1199.05	2.56	πnear Q
A'	286.53	287.10	1197.30	0.46	free-electron-like interlayer states + adsorption
A''	288.40	288.72	1195.68	1.10	free-electron-like interlayer states + adsorption
A'''	288.70	289.94	1194.46	0.0	free-electron-like interlayer states + adsorption
A''''	290.70	290.72	1193.68	0.52	free-electron-like interlayer states + adsorption
C-H Exc.	291.76	291.77	1192.63	0.67	Exciton
B	292.65	292.60	1191.80	1.82	σ_1, σ_2: $\Gamma \rightarrow$Q
C	295.50	294.55	1189.85	6.23	π_0 or π_1 near Γ
D	297.80	298.75	1185.65	2.00	/
P''	297.51	297.51	1186.89	0.0	Potassium L_2 level
E	303.50	301.42	1182.98	3.86	σ_7 near Q
F	307.50	306.60	1177.80	3.15	σ_9 near Q
G	308.50	309.55	1174.85	1.97	/
H	316.50	315.20	1169.20	0.33	π_4 near Q
I	329.00	329.00	/	/	/
J	333.00	333.00	/	/	/
P	296.60	297.30	1187.10	0.19	Potassium L_2, L_3 level
P'	299.83	299.81	1184.59	0.17	Potassium L_2-L_1 levels

Unannealed contaminated CNSs spectra

It is observed that some features present in Figure 14.7 are not found in Figures 14.8 and 14.9 especially peaks K and L, and are replaced by P, P' and P". These new peaks are not intrinsic to CNTs. The peaks P', P'' and P''' not prominent in figure 14.8 are particularly important in figure 14.9.

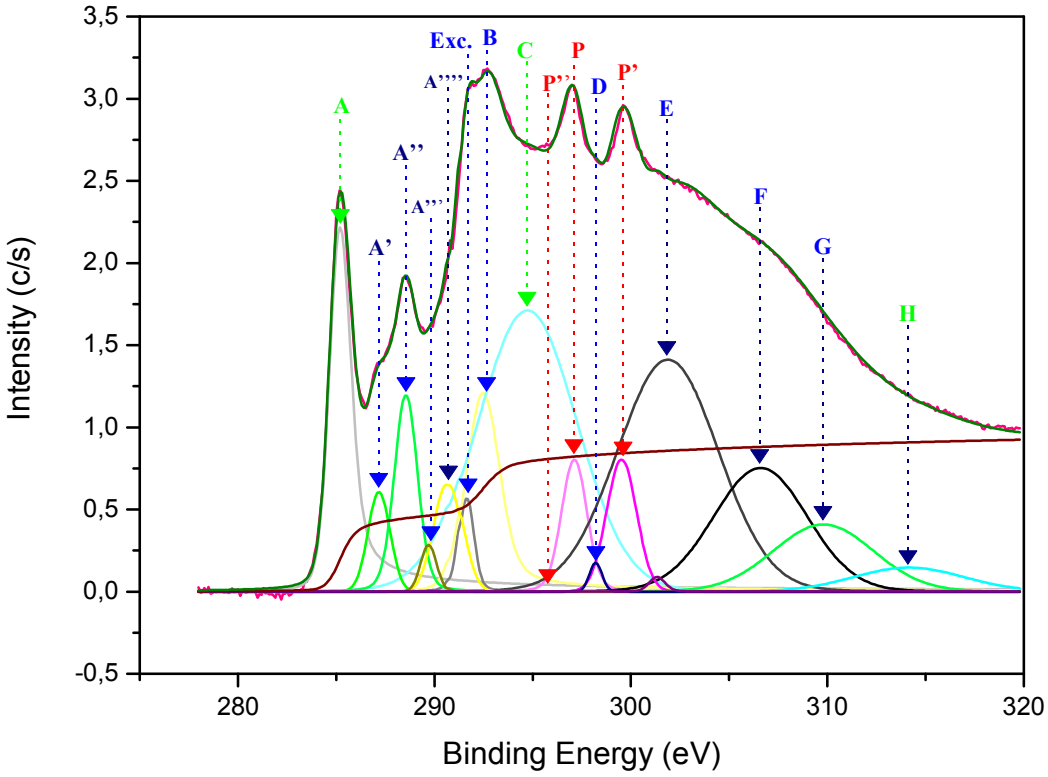

FIGURE 14.9
Potassium contaminated CNTs experimental and calculated superimposed XANES spectra at normal incidence from an unannealed sample

They are non intrinsic and result of contamination of atoms, molecules or radical compounds, in agreement with SEM and TEM analysis, where it is not found bundles of CNTs as it may be according to literature and the surface of CNSs seems not clear. Among the reasons of the presence of non-intrinsic features in XANES spectra is the presence of TM particles as proved by SEM and TEM. Actually, it is known that the features attributed to the so-called free-electron-like interlayer states in the graphite and other carbon nanostructures are also due to contamination [54, 55]. The peaks P, P' and P" are assigned to adsorbed potassium atoms according to features parameters [55, 65].

TABLE 14.6
Main features' parameters for CNTs XANES spectra at normal incidence for unannealed contaminated CNSs

Unannealed and potassium-contaminated CNTs at normal					
Peaks' Names	Peaks	Binding energy (eV)	Kinetic energy (eV)	Intensity (c/s)	Final-state band and Brillouin-zone
A	285.50	285.20	1199.20	3.05	π_0 near Q
A'	286.53	287.40	1197.00	0.61	free-electron-like interlayer states + adsorption
A''	288.40	288.55	1195.85	2.44	free-electron-like interlayer states + adsorption
A'''	288.70	289.94	1194.46	0.83	free-electron-like interlayer states + adsorption
A''''	290.70	291.00	1193.40	1.52	free-electron-like interlayer states + adsorption
C-H Exc.	291.76	291.80	1192.60	0.43	Exciton
B	292.65	292.42	1191.98	2.72	σ_1, σ_2: $\Gamma \rightarrow$Q
C	295.50	294.10	1190.30	4.01	π_0 or π_1 near Γ
D	297.80	298.52	1185.88	0.43	/
P''	297.51	297.51	1186.89	0.60	Potassium L2 level
E	303.50	301.55	1182.85	5.08	σ_7 near Q
F	307.50	306.50	1177.90	2.00	σ_9 near Q
G	308.50	308.70	1175.70	1.40	/
H	316.50	313.50	1170.90	0.75	π_4 near Q
I	329.00	329.00	/	/	/
J	333.00	333.00	/	/	/
P	296.60	296.60	1187.80	1.70	Potassium L2, L3 level
P'	299.83	299.83	1184.57	0.95	Potassium L2-L1 levels

XANES Spectra of CNSs at grazing incidence

Pristine CNSs

At grazing incidence, pristine CNSs XANES spectra, shown in figure 14.10, have the same features as in normal incidence. The only difference occurring is relative difference in peaks intensities. The energies and assignments of the main peaks in the Carbon K-edge spectra of pristine are summarized in table 14.7. The two prominent peaks near 285.5 eV (A) and 292.5 eV (B) are known to be associated with an unoccupied π^* band or 'white band' and σ^* band, respectively]. The C spectral feature at 293.77 eV corresponds to a π -symmetry. The D, E and F peaks around 297.8, 305.5 and 307.5 eV, respectively, are correlated to σ -symmetry.

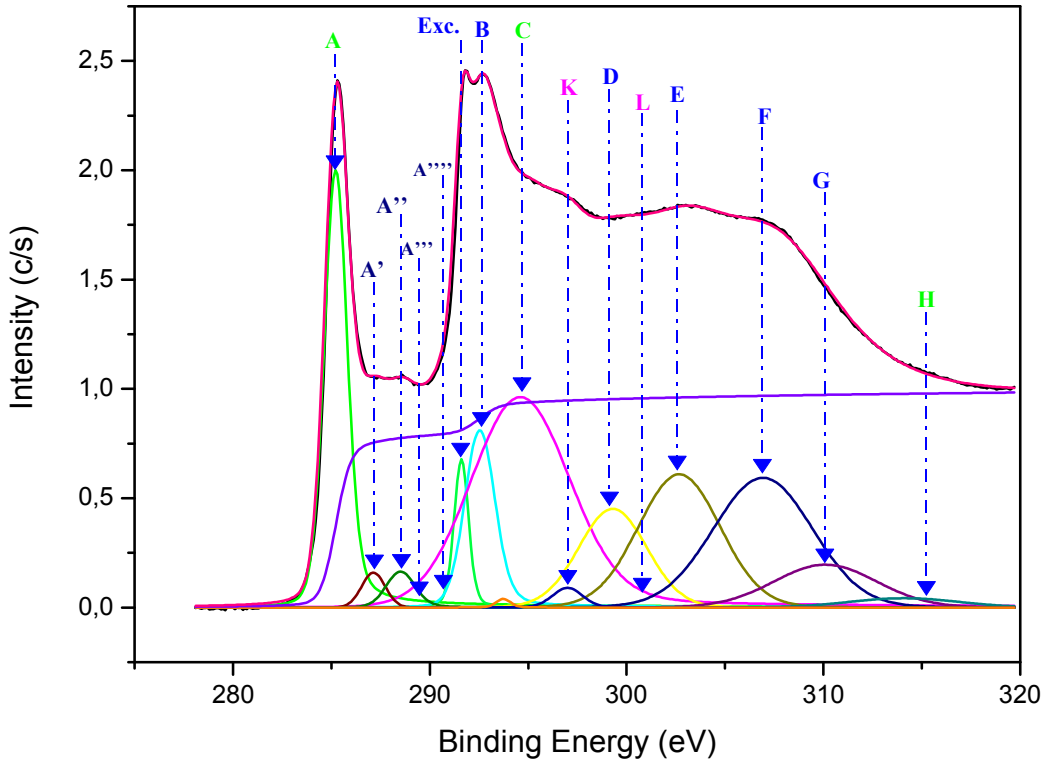

FIGURE 14.10
CNSs experimental and calculated superimposed XANES spectra at grazing incidence from the CNTs Annealed sample

The H peak at 316.5 eV corresponds to π -symmetry. For peaks G, I and J, respectively, at 308.5, 329 and 333 eV in [51], an unambiguous determination of the symmetry was not possible from the XANES spectra. Inadequate energy resolution and uncertain normalization result in uncertainties in the peak intensities. In good agreement with the literature studies, the spectra are dominated by the σ ∗ - and σ -C π∗- bands, and the σ -symmetry final-state structures B, D, E and F are well resolved. The H π -symmetry final state observed at grazing incidence and located at 316.5 eV has completely disappeared at normal incidence. The σ -C H∗ exciton at 292 eV and the FELI states at 286.5 and 288.5 eV are well resolved.

TABLE 14.7
Main features' parameters for CNTs XAS spectrum at grazing incidence from non contaminated CNSs

CNTs at grazing incidence					
Peaks' Names	Peaks	Binding energy (eV)	Kinetic energy (eV)	Intensity (c/s)	Final-state band and Brillouin-zone
A	285.50	285.20	1199.20	3.55	π_0 near Q
A'	286.53	287.14	1197.26	0.24	free-electron-like interlayer states + adsorption
A''	288.40	288.50	1195.90	0.40	free-electron-like interlayer states + adsorption
A'''	288.70	/	/	/	free-electron-like interlayer states + adsorption
A''''	290.70	/	/	/	free-electron-like interlayer states + adsorption
C-H Exc.	291.76	291.65	1192.75	0.68	Exciton
B	292.65	292.57	1191.83	1.93	σ_1, σ_2: $\Gamma \rightarrow Q$
C	295.50	294.50	1189.90	6.54	π_0 or π_1 near Γ
D	297.80	297.06	1187.34	0.45	σ_3–σ_6: $Q \rightarrow P$
E	303.50	302.70	1181.70	3.83	σ_7 near Q
F	307.50	306.97	1177.42	4.00	σ_9 near Q
G	308.50	309.75	1174.65	1.90	/
H	316.50	315.40	1169.00	1.20	π_4 near Q
I	329.00	329.00	/	/	/
J	333.00	333.00	/	/	/
K	295.40	297.05	1187.35	0.00	π_0 or π_1 near Γ
L	301.85	299.30	1185.10	2.40	σ_6–σ_7: near Q

Annealed contaminated CNSs

With prior annealing of samples the increase of intensity in the FELI states band region of the spectra is prevented. Figure 14.11 shows the main features of XANES annealed spectra of potassium CNTs contaminated in grazing incidence. The π^* antibonding state corresponds physically to the out-of-plane bonds in the sp^2 bonding configuration (indicating the presence of unsaturated carbon–carbon interactions) and exhibits strong polarization dependence. The different main features are presented in table 14.8.

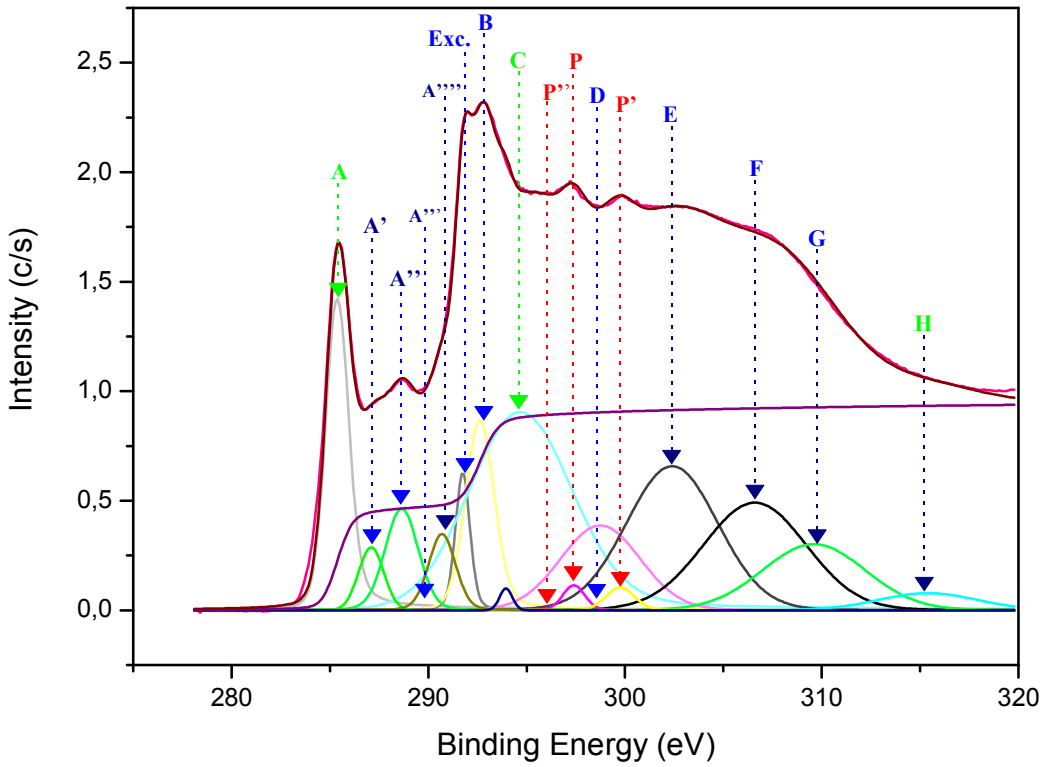

FIGURE 14.11
Potassium contaminated CNTs experimental and calculated superimposed XAS spectra at grazing incidence from the annealed sample of CNTs

The presence of a σ∗ exciton at 292 eV points to a material with well-formed local bonding configuration or good short-range order and exhibits long-range disorder. The planar graphite sheets in the nanotubes are bent into a cylinder. While varying the diameter of the CNTs, the intensities of the π∗ -band and interlayer-states features are enhanced relative to those of HOPG with a decrease of the CNT diameter. The increase of the near-edge feature intensities with the decrease of the CNT diameter suggests that both the C2p orbitals lose more charge to the 3d orbitals of the catalyst transition metal (TM) atoms: nickel, cobalt and iron, for smaller-diameter CNTs and the presence of surface contaminants.

TABLE 14.8
Main features' parameters for annealed and potassium-contaminated CNTs XAS spectrum at grazing incidence

Annealed and potassium-contaminated CNTs at grazing incidence					
Peaks' Names	Peaks	Binding energy (eV)	Kinetic energy (eV)	Intensity (c/s)	Final-state band and Brillouin-zone
A	285.50	285.35	1199.05	2.56	π_0 near Q
A'	286.53	287.10	1197.30	0.46	free-electron-like interlayer states + adsorption
A''	288.40	288.652	1195.75	1.02	free-electron-like interlayer states + adsorption
A'''	288.70	289.94	1194.46	0.0	free-electron-like interlayer states + adsorption
A''''	290.70	290.70	1193.70	0.63	free-electron-like interlayer states + adsorption
C-H Exc.	291.76	291.75	1192.65	0.64	Exciton
B	292.65	292.60	1191.80	1.82	σ_1, σ_2: $\Gamma \rightarrow$Q
C	295.50	294.58	1189.82	6.40	π_0 or π_1 near Γ
D	297.80	298.75	1185.65	2.00	/
P''	297.51	297.51	1186.89	0.0	Potassium L_2 level
E	303.50	302.40	1182.00	3.88	σ_7 near Q
F	307.50	306.60	1177.80	3.26	σ_9 near Q
G	308.50	309.60	1174.80	2.00	/
H	316.50	315.40	1169.00	0.50	π_4 near Q
I	329.00	329.00	/	/	/
J	333.00	333.00	/	/	/
P	296.60	297.40	1187.00	0.17	Potassium L_2, L_3 level
P'	299.83	299.76	1184.64	0.20	Potassium L_2-L_1 levels

Unannealed contaminated CNSs

The observations are the same for unannealed samples in normal incidence. Non-intrinsic prominent peaks P, P' and P" are present in figure 14.12 in agreement with SEM and TEM analysis, where it is not found bundles of CNTs as it may be according to literature and the surface of CNSs are unclear. Among the reasons of the presence of non-intrinsic features in XANES spectra is the presence of TM particles as proved by SEM and TEM.

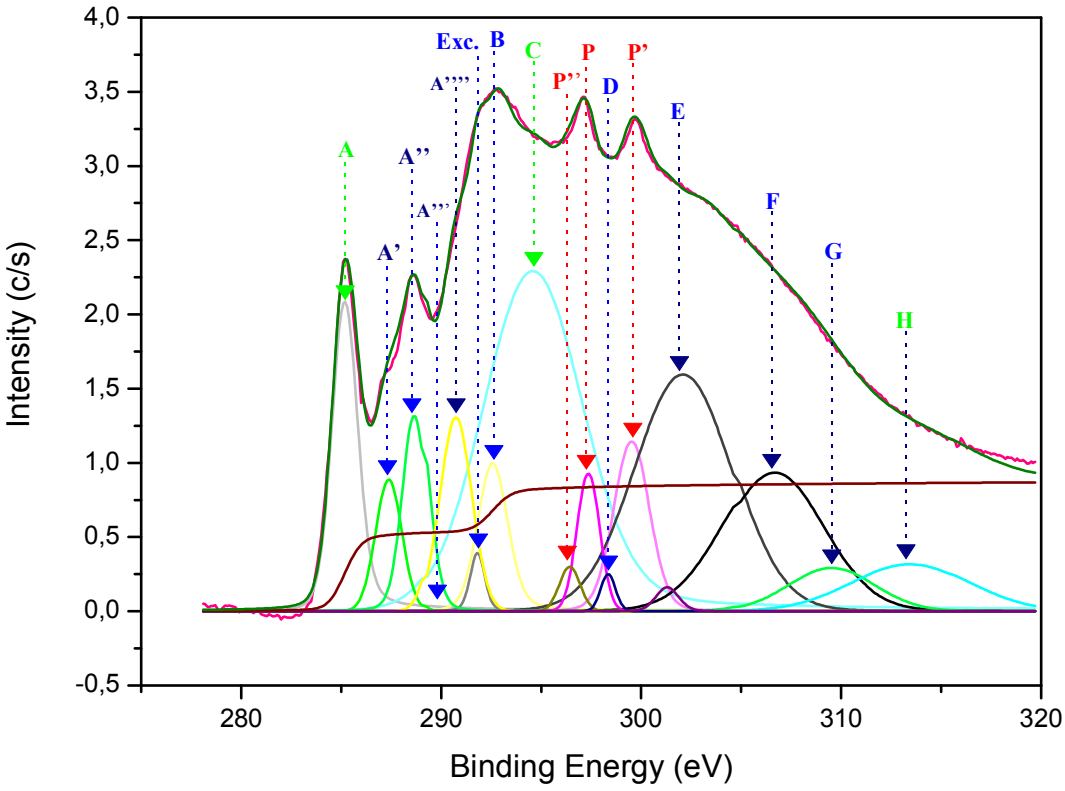

FIGURE 14.12
Potassium contaminated CNTs experimental and calculated superimposed XANES spectra at grazing incidence from an unannealed sample

Actually, it is known that the features attributed to the free-electron-like interlayer states in the graphite and other carbon nanostructures are also due to contamination [1, 2, 54, 55]. The peaks P, P' and P" are assigned to adsorbed potassium atoms according to features parameters [55, 65].

TABLE 14.9
Main features' parameters for unannealed and potassium-contaminated CNTs XAS spectrum at grazing incidence

Unannealed and potassium-contaminated CNTs at grazing incidence					
Peaks' Names	Peaks	Binding energy (eV)	Kinetic energy (eV)	Intensity (c/s)	Final-state band and Brillouin-zone
A	285.50	285.25	1199.15	2.10	π_0 near Q
A'	286.53	287.55	1196.85	0.95	free-electron-like interlayer states + adsorption
A''	288.40	288.73	1195.67	3.85	free-electron-like interlayer states + adsorption
A'''	288.70	289.96	1194.44	0.85	free-electron-like interlayer states + adsorption
A''''	290.70	290.95	1193.45	1.95	free-electron-like interlayer states + adsorption
C-H Exc.	291.76	291.94	1192.46	0.46	Exciton
B	292.65	292.44	1191.96	3.43	σ_1, σ_2: $\Gamma \rightarrow Q$
C	295.50	294.23	1190.17	4.75	π_0 or π_1 near Γ
D	297.80	298.47	1185.93	0.38	/
P''	297.60	297.60	1186.80	0.57	Potassium L_2 level
E	303.50	301.62	1182.78	5.27	σ_7 near Q
F	307.50	306.40	1178.00	2.07	σ_9 near Q
G	308.50	308.70	1175.70	1.40	/
H	316.50	313.50	1170.90	0.93	π_4 near Q
I	329.00	329.00	/	/	/
J	333.00	333.00	/	/	/
P	296.65	296.65	1187.75	1.80	Potassium L_2, L_3 level
P'	299.68	299.68	1184.72	1.32	Potassium L_2- L_1 levels

Impact of contamination

Since the discovery of carbon novel materials [34, 66], much success is expected from numerous applications due to incredible properties such as physical strength, high conductivity, high aspect ratio and chemical stability. In recent research, it has been shown that, Carbon nanotubes for example, has its electrical resistivity changed sensitively on exposure to gaseous ambient containing molecules of O_2, NO_2, NH_3 or biomolecules [67]. Perfect CNSs are an abstraction or a creation of the mind, because of the hexagonal structure of sp^2 carbon atoms, which form the layers, have always alterations during the manufacturing or the purification processes. Careful observations of TEM in high resolution imaging show mainly surface complexities due to materials adsorbed on their outside walls or incorporated into the cylindrical hollows. These defects are important because they often modify the electronic properties or other properties of the nanostructures, and can influence their applications. 'SWCNTs come often as tightly bundles entangled as curly locks" is seen in literature, but the packing of

the nanotubes inside bundles is not observed according to SEM images, in specific case helping to differentiate SWCNTs from MWCNTs. CNTs are simply observed in SEM images as tubes with poorly, medium or highly orientation. The poor degree of this orientation is precluding nanotubes to form bundles. Among the reasons of this situation is contamination. Adsorbed compounds create a particular environment not propitious to bundles formation by its bulk. As consequence, many theoretical properties of SWNTs will not be found in such sample. The bundling of nanotubes during the processing is an important factor for many applications such as electrical and thermal transport. CNTs bundles are also of great interest as a X-ray refractory lens.

Generally, the presence of defects, contaminants or any impurities, alters nanomaterial's properties such as mechanic strength and chemical reactivity. In reduced dimensions as nanoscale, defects play most significant roles and can dominate physical properties. Such consequences are critically important to the field of nanoscience, in which low dimensional materials are synthesized, characterized, and integrated for applications. The vacancy initially results in dangling bonds for example, will immediately rehybridize or react with surrounding molecules. Theoretical effort has focused on how the dangling bonds associated with one or more vacancies might serve as sites for interconnecting nanotubes, providing chemical reactivity. CNSs surfaces interact with adsorbed gases, moisture, supporting substrates, and nearby amorphous carbons, all of which provide spontaneous reaction pathways to saturate dangling bonds. In all but ultrahigh vacuum conditions, most intermediates are susceptible to nucleophilic attack by H_2O, making –OH terminated vacancies one of the most likely, and physically relevant configurations.

XANES spectra present features with prominent peaks due to non-intrinsic bonds. These bonds are formed when chemical compounds or molecules are adsorbed in sample sidewalls. An appropriate study shows that the behaviour of samples is quiet closer to its characteristics notably its curvature or outer diameter [2]. For example SWNTs spectra have their prominent peaks kept during thermal annealing processes as shown in figure 14.13. The comparison of XANES spectra of different samples of carbon nanostructures: pristine samples, annealed and unannealed samples shows other important differences. These differences are due once more to the varying behaviour of carbon nanostructures samples in presence of contaminants. In the typical case of CNSs, when the outer diameter is important, the CNSs are less chemically active and therefore are not favoured to establish chemical bonds [2]. But with small outer diameter as in the case of Single Walled carbon nanotubes, the presence of contaminants in sidewall is very important and of course the process of purification is too heavy.

In Brief, the phenomenon of contamination is very important depending of the specific properties of carbon nanostructure. Those with a great curvature for example react and bond strongly with contaminants than other. So the solution of the problem of contamination may depend of specificities of each carbon nanostructure.

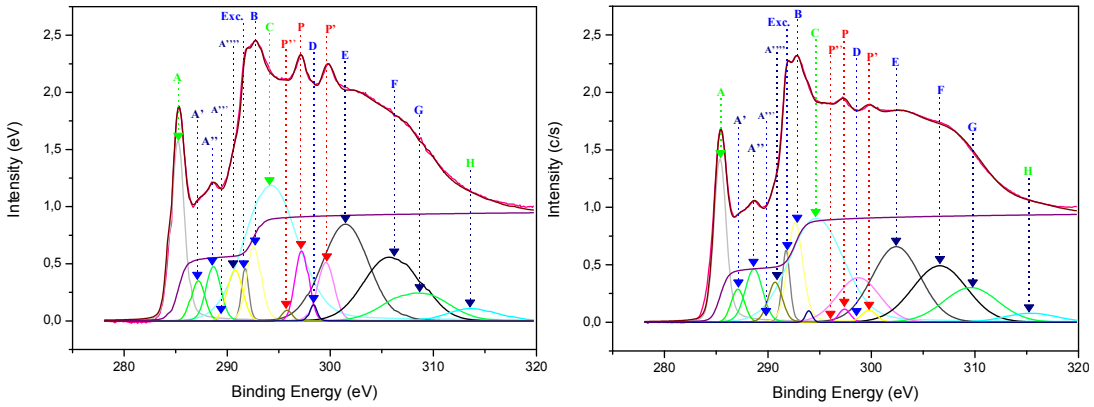

(a) (b)

FIGURE 14.13
Difference of behaviour with contaminants between SWCNT (a) and MWCNT (b). In spite of thermal annealing peaks remain prominent in SWCNT spectra explaining the importance in term of presence of contaminants

Conclusions

Fundamental understanding of interactions between X-rays and matter provides rich information of nanomaterials. Carbon nanostructures through a systematic investigation are subject of unique properties. But realistic CNSs samples are often subject to undesirable contaminants adsorbed on sidewall. XANES spectroscopy as one of techniques using interaction X-rays and matter, is a powerful tool to provide local information on the environment around carbon material atoms, in diamond, amorphous carbon and nitride amorphous graphitic carbon. It is also suitable to probe the adsorption of any functional groups and thus probe the quality of CNSs. XANES spectra of CNSs helped to investigate the presence of contaminants and other impurities in sidewall. The phenomenon seems remarkably important according to XANES spectra analyzed. Thus, a great effort need to be done in order to reduce as much as possible, the gap between theoretical and practical properties of carbon nanostructures by minimizing contamination effects. Therefore the manufacturing operators must multiply efforts to avoid or reduce this accidental phenomenon. Understanding the mechanism of contamination and its importance in manufacturing of carbon nanomaterials is among the key of matching theoretical and practical or experimental marvelous properties of these novel building blocks, for the requirements in applications. Characterization of CNSs either for applications or adsorption studies is very important. There are two main reasons. Carbon nanostructures may contain a number of impurities depending on the method of production and subsequent purification technique used under relevant environmental conditions. The adatoms, compounds or molecules generated from the manufacturing environment need to be controlled or destroyed to avoid their adsorption; Interdisciplinary efforts are to be sought to overcome the limitations of current nanomanufacturing processes and to produce carbon nanostructures that are contaminant-free.

Carbon nanostructures in general and carbon nanotubes in particular have unique properties. These unique properties lead to the fabrication of different devices. The improvements of current synthesis techniques of carbon nanostructures needed to make available commercial contaminant-free products. These qualify carbon nanostructures may construct a totally new nanotechnology architecture.

Acknowledgements

The author would like grateful acknowledge Pr Ousmanou Motapon, Pr Mohamadou Alidou and Pr Jeannot Mane Mane for their useful discussions.

References

1. J. Zhong, C. Liu, Z. Y. Wu, A. Mamatimin, I. Kurash, H. M. Cheng, B. Gao, L. Liu, "XANES Study of Carbon Based Nanotubes", *High Energy Physics and Nuclear Physics*, **29** (2005), 97.
2. R. Eba Medjo, B. Thiodjio Sendja, J. Mane Mane and P. Owono Ateba, "A study of carbon nanotube contamination by XANES spectroscopy", *Phys. Scr*., **80**, 4, (2009), 045601.
3. B. Pan and B. Xiang, "Mechanisims of Organic Chemicals on Carbon Nanotubes", *Environ. Sci. Technol*. **42**, 24 (2008) 9005-9013.
4. A. Dabrowski, "Adsorption - from theory to practice", *Adances in Colloid and Interface Science* **93** (2001) 135-224
5. M. Burghard, "Electronic and vibrational properties of chemically modified single-wall carbon nanotubes", *Surf. Sci. Rep*. **58** (2005) 1-109.
6. H. Hu, B. Zhao, M.A. Hamon, K. Kamaras, M.E. Itkis and R.C. Haddon, "Sidewall functionalization of single-walled carbon nanotubes by addition of dichlorocarbene"*., J. Am. Chem. Soc*. **125** (2003) 14893-900.
7. A. López-Bezanilla, F. Triozon, S. Latil, X. Blasé and S. Roche, "Effect of the chemical functionalization on charge transport in carbon nanotubes at the mesoscopic scale"., *Nano Lett.* **9** (2009) 940-4.
8. M.S. Strano, C.A. Dyke, M.L. Usrey, P.W. Barone, M.J. Allen, H. Shan, et al., "Electronic structure control of single-walled carbon nanotube functionalization"*, Science.* **301** (2003) 1519-22.
9. K. Balasubramanian and M. Burghard, "Chemically functionalized carbon nanotubes"., *Small*. 1 (2005) 180-92
10. W. Chen, L. Duan and D.Q. Zhu, Adsorption of polar and nonpolar organic chemicals to carbon nanotubes, Environ. Sci. Technol. **41**, (2007) 8295-8300.
11. K. Yang, X. L. Wang, L. Z. Zhu and B. S. Xing*, "*Competititve sorption of pyrene, phenanthrene and naphthalene on multiwalled carbon nanotubes", *Environ. Sci. Technol*. **40**, (2006) 5804-5810.
12. M. S. Dresselhaus, G. Dresselhaus and P. C. Eklund, *Science of Fullerene and Carbon Nanotubes*, Academic Press, (1996).
13. T. W. Ebbesen, Carbon Nanotubes: *Preparation and Properties, Chemical Rupper Corp*, Boca Raton, FL, (1997).
14. R. Khare and S. Bose, Carbon Nanotube Based Composites- A Review, *Journal of Minerals & Materials Characterization & Engineering*, **4**, 1, (2005), 31-46.
15. E.-S. Park, Preparation, Characterization and Applicability of Covalently Functionalized MWNT,in *Physical and Chemical Properties of Carbon Nanotubes* Ed. Satoru Suzuki, ISBN 978-953-51-1002-1016, (2013).
16. P. Singh, R. M. Tripathi and A. Saxena, Synthesis of carbon nanotubes and their biomedical applications. Journal of Optoelectronics and Biomedical Materials, **2**, (2010), 91-98.
17. R. Q. Zhang and A. D. Sarkar, Theoretical Studies on Formation, Property Tuning and Adsorption of Graphene Segments, *Physics and Applications of Graphene - Theory*, Ed. Sergey Mikhailov, ISBN 978-953-307 (2011) 152-157.

18. A. Zhimin, J. Yang and S. Li, Applications of Al Modified Graphene on Gas Sensors and Hydrogen Storage, *Physics and Applications of Graphene - Theory*, Ed. Sergey Mikhailov, ISBN 978-953-307 (2011) 152-157.
19. P. V. Kamat, Meeting the Clean Energy Demand: Nanostructure Architectures for Solar Energy Conversion, *J. Phys. Chem. C*, **111** (2007), 2834-2860.
20. K. Sears, L. Dumée, J. Schütz, M. She, C. Huynh, S. Hawkins, M. Mikel and S. Gray, Recent Developments in Carbon Nanotube Membranes for Water Purification and Gas Separation, *Materials*, **3**, (2010), 127-149.
21. H. Guan Ong and J. Wang, Study of Carbon Nanotube Based Devices Using Scanning Probe Microscope, in *Physical and Chemical Properties of Carbon Nanotubes* Ed. Satoru Suzuki, ISBN 978-953-51 -2013) 1002-1006.
22. L. Banyai, S. W. Koch, Semiconductor quantum Dots, *World Scientific Publishing Co*.: River Edge, NJ (1993).
23. V.L. Colvin, *Clean water from small materials in Nanotechnology of the environment MRS*: Boston MA (2007).
24. M. S. Dresselhaus, G. Dresselhaus and P. Avouris, *Carbon Nanotubes: Synthesis, Structure, Properties and Applications* vol 29 Berlin: Springer (2001).
25. C. Y. Zhi, X. D. Bai, E. G. Wang, "Enhanced Field Emission from Carbon Nanotubes by Hydrogen Plasma Treatment.". *Appl. Phys. Lett*., **81**, (2002) 1690.
26. P.M. Ajayan, O.Z. Zhou, « *Carbon Nanotubes », Topics Appl. Phys.*, Eds: M.S. Dresselhous, G. Dresselhous, Ph. Avouris, **80**, pp. 391-425 (2001).
27. Delziet L., Nguyen C., Stevens R., Han J., Meyyappan M., "Growth of Carbon Nanotubes by Thermal and Plasma Chemical Vapor Deposition Processes and Applications in Microscopy », *Nanotech*., **13**, (2002) 280.
28. Kind H., Bonard J.-M., Emmenegger C., Nilsson L.-O., Hernadi K., Maillard-Schaller E., Schlapbach L., Forro L., Kern K., "Patterned Films of Nanotubes Using Microcontact Printing of Catalysts", *Adv. Mater*., **11**, (1999) 1285.
29. [29] Kong J., Cassell A. M., Dai H., "Chemical Vapor deposition of methane for single-walled carbone nanotubes", *Chem. Phys. Lett.*, **292**, (1998) 567.
30. Sugie H., Tanemura M., Filip V., Iwata K., Takahashi K., Okuyama F., "Carbon Nanotubes as electron source in X-ray tube" Appl. Phys. Lett. **78**, (2001) 2578.
31. T. W. Ebbesen and P. M. Ajayan, Large-scale synthesis of carbon nanotubes, *Nature*, **358** (1992), 220-222.
32. V. Ivanov, J. B. Nagy, P. Lambin, A. Lucas, X. B. Zhang, X. F. Zhang, D. Bernaerts, G. Van Tendeloo, S. Amelinckx and J. Van Landuyt, Carbon nanotubes production by catalytic pyrolysis of benzene, *Chem. Phys. Lett.* **223** (1994) 329.
33. R. Eba Medjo, Carbon Nanotubes Synthesis, *Carbon Nanotubes Applications on Electron Devices*, Ed. Jose Mauricio Marulanda. ISBN 978-953-307-496-2 www.intechopen.com (2011).
34. H. W. Kroto H, J. R. Heath, S. C. O'Brien, R. F. Curl and R. F. Smalley, "C_{60} Burkminsterfullerene", *Nature*, **318** (1985)162.
35. A. M. Rao A, S. Bandow, E. Richter, P. C. Eklund, "Raman spectroscopy of pristine and doped single wall nanotubes », *Thin Solid Films*, **331**, 141, 1998.
36. Y. Zhang, H. Gu, K. Suenaga, S. Iijima, « Heterogeneous growth of B–C–N nanotubes by laser ablation », *Chem. Phys. Lett*. **279**, 264, 1997.
37. M. H. Rummeli, C. Kramberger, M. Loeffler, O. Jost, M. Bystrzejewski, A. Grueneis, T. Gemming, W. Pompe, B. Buechner and T. Pichler, "Catalyst volume to surface area constraints for nucleating carbon nanotubes", *J. Phys. Chem. B*, **111**, (2007) 8234.

38. S. Amelinckx, D. Bernaerts, X. B. Zhang, G. Van Tendeloo and J. Van Landuyt, "A structure model and growth mechanism for multishell carbon nanotubes", *Science*, **267**, (1995) 1334.
39. O. Jost, A. Gorbunov, X. Liu, W. Pompe and J. Fink, "Single-walled carbon nanotube diameter", *J. Nanosci. Nanotechnol.,* 4 (2004) 433.
40. J. M. Lambert, P. M. Ajayan, P. Bernier, "Synthesis of Single and Multishell Carbon Nanotubes", Synthetic *Metals*, **70**, 1475, 1995.
41. W. Merchan-Merchan, A. V. Saveliev, L. A. Kennedy, A. Fridman, "Formation of Carbpn nanotubes in counter-flow oxy-methane diffusion flames without catalysts", *Chemical Physics Letters;* **354**, 20, 2002.
42. W. Merchan-Merchan, A. V. Saveliev, L. A. Kennedy, "High-rate flame synthesis of vertically aligned carbon nanotubes using electric field control", *Carbon,* **42**, 599, 2004.
43. H. Okuno, J.-P. Issi, J.-C.Charlier, "Catalyst assisted synthesis of carbon nanotubes using the oxy-acetylene combustion flame method", *Carbon* **43**, 864, 2005.
44. A. J. Bard, F. R. F. Fan, J. Kwak , O. Lev, "Scanning electrochemical microscopy. Introduction and principles", *Anal. Chem*., **61** (1989) 132.
45. R. A. Wallingford, A. G. Ewing, "Capillary Zone Electrophoresis with Electrochemical Detection", *Anal. Chem*. **59** (1987) 1762.
46. M. Breing, M. H. Chen, G. E. Ice G, F. Parente, B. Crasemann, G. S. Brown,"Atomic inner-shell level energies determined by absorption spectrometry with synchrotron radiation", *Phys. Rev. A* **22** (1980).
47. C. M. Teodorescu, R. C. Karnatak, J. M. Esteva, A. El Afif, P-P. Connerade, "Unresolvable Rydberg lines in x-ray absorption spectra of free atoms", *J. Phys. B*, **26** (1993) 4019.
48. D. C. Koningsberger and R. Prins, *X-Ray Absorption – Principles, Applications, Techniques of EXAFS, SEXAFS and XANES*, Wiley-Interscience, New-YorK (1992).
49. D. C. Koningsberger and R. Prins, *X-Ray Absorption – Principles, Applications, Techniques of EXAFS, SEXAFS and XANES, Chemical Analysis*, **92**, Wiley (1988).
50. G. Comelli, J. Stohr, W. Jark, B. B.Pate, "Extended X-ray absorption fine-structure-studies of diamond and graphite", *Phys Rev. B*, **37** (1988) 438.
51. R. A. Rosenberg, P. J. Love and V. Rehn, Polarization-dependant C(K) near-edge X-ray absorption fine structure of graphite, *Phys. Rev. B* **33** (1986) 4034.
52. P. E. Batson, "Carbon 1 s near-edge-absorption fine structure in graphite", *Phys. Rev. B*, **48**, 2608, 1993.
53. D. A. Fischer, R. M. Wentzcovitch, P. G. Carr, A. Continenza, A. J. Freeman, "Graphitic interlayer states: A carbon k near-edge x-ray absorption fine-structure study", *Phys. Rev. B* **44** (1991) 1427.
54. D. Pacile, M. Papagno, A. F. Rodriguez, M. Grioni, L. Papagno, C. O. Girit, J. C. Meyer, G. E. Begrtrup, and A. Zettl, "Near edge x-ray absorption fine-structure investigation of graphene," *Phys. Rev. Lett.,* **101**, (2008) 066806.
55. R. Eba Medjo, Characterization of Carbon Nanotubes, *Physical and Chemical Properties of Carbon Nanotubes*, Ed. Satoru Suzuki. IBN 980 - 953 – 309 – 536 – 0 www.intechopen.com, 2013.
56. R. Eba Medjo, B. Thiodjio Sendja, J. Mane Mane and P. Owono Ateba, XAS study of the orientation of oriented carbon nanotubes films, *Phys. Scr.*, **80**, 5, (2009), 055602.
57. L. Grigorian, G. U. Sumanasekera, A. L. Loper, S. L. Fang, J. L. Allen, P. C. Eklund, *Phys. Rev. B*, **60** (1999) R11309.
58. D. M. Duffy and J. A. Blackman, *Phys. Rev. B*, **58** (1998) 7443.
59. J. W. Mintmire, B. I. Dunlap, C. T. White, *Phys. Rev. Lett*., **68** (1992) 631.
60. V.P. Dravid, X. Lin, Y. Wang, X. K. Wang, A. Yee, J. B. Ketterson, R. P. H. Chang, "Buckytubes and derivatives: Their growth for buckyball formation", *Science*, **259** (1993) 1601.

61. D. A. Fischer, R. M. Wentzcovitch, P. G. Carr, A. Continenza, A. J. Freeman, “Graphitic interlayer states: A carbon k near-edge x-ray absorption fine-structure study”, *Phys. Rev. B* **44** (1991)1427.
62. G. Stan and M. W. Cole, “Low coverage adsorption in cylindrical pores”, *Surface Science*, **395** (1998) 280
63. M. Eswaramoorthy, R. Sen and C. N. R. Rao, "A Study of Micropores in Single-Walled Carbon Nanotubes by the Adsorption of Gases and Vapors", *Chem. Phys. Lett.* **304** (1999) 207.
64. M. W. Cole and E. S. Hernandez, "Unified model of wetting and pore-filling,"*Physical Review B* **75** (2007).
65. S. Sasaki, KEK, National Laboratory for High Energy, Physics, *Report*, **83** (1984) 22.
66. S. Iijima, “Helical microtubules of graphitic carbon”, *Nature,* **354**, (1991) 56.
67. A.Star, J.-C. Gabriel, K. Bradley, G. Gruner, “Electronic detection of specific protein binding using nanotube FET devices,” *Nano Lett.,* **3**, (2003) 459.